

# N-Body Simulations of Collective Effects in Spiral and Barred Galaxies

Xiaolei Zhang

*School of Physics, Astronomy, and Computational Sciences, George Mason University,  
4400 University Drive, Fairfax, VA 22030, USA, xzhang5@gmu.edu*

---

## Abstract

We present gravitational N-body simulations of the secular morphological evolution of disk galaxies induced by density wave modes. In particular, we address the demands collective effects place on the choice of simulation parameters, and show that the common practice of the use of a large gravity softening parameter was responsible for the failure of past simulations to correctly model the secular evolution process in galaxies. We also demonstrate that the secular evolution rates measured in our improved simulations agree to an impressive degree with the corresponding rates predicted by the recently-advanced theories of dynamically-driven secular evolution of galaxies. The results of the current work, besides having direct implications on the cosmological evolution of galaxies, also shed light on the general question of how irreversibility emerges from a nominally reversible physical system.

*Keywords:* galaxies: evolution; galaxies: structure; galaxies: spiral

---

## 1. INTRODUCTION

### 1.1. *Self-Organization in Nonequilibrium Systems*

Understanding the self-organization behavior of nonlinear, far from equilibrium systems is among the most challenging of problems of contemporary research. This multi-disciplinary study is relevant to answering many key questions in condensed matter physics, biological and life sciences, social sciences, as well as the processes of structure formation in the universe.

Several leading scientists of the 20th century considered the exploration of collective behaviors or the processes of morphogenesis to be of central importance to the future advancement of science. More than half a century ago,

Richard Feynman closed volume II of “The Feynman Lectures on Physics” by declaring: “The next great era of awakening of human intellect may well produce a method of understanding the qualitative content of equations. Today we cannot. Today we cannot see that the water flow equations contain such things as the barber pole structure of turbulence that one sees between rotating cylinders. Today we cannot see whether Schrodinger’s equation contains frogs, musical composers, or morality – or whether it does not” (Feynman, Leighton, & Sands 1964). P.W. Anderson, a noted condensed matter physicist, penned an influential article for *Science* entitled “More is different” (Anderson 1972), in which he called attention to the hierarchical organization of physical systems, and the ability of many-degrees-of-freedom systems to form emergent structures and dynamics which break the symmetries of equations describing the underlying micro-dynamics.

Among the studies on morphogenesis, one of the most prophetic is that of Ilya Prigogine. In his theory of “dissipative structures”, Prigogine emphasized the entropy-production-enhancing function of self-organized global patterns in far-from-equilibrium systems, as well as the constructive role of dissipation in maintaining these patterns (Prigogine 1980). To paraphrase this theory, most of the self-organized structures in nature come in roughly two types: (1) equilibrium structures, which are formed through equilibrium phase transitions. The examples of equilibrium structure formation include the phase transition of water to form ice when the temperature is lowered to zero degree Celsius, as well as the formation of minerals of a specific crystal structure when the environmental temperature and pressure satisfy a range of conditions (i.e. the formation of diamond crystal from carbon in a high pressure environment). (2) nonequilibrium structures, which are formed in systems far from equilibrium, and which (in addition to sharing some common features with structures formed in equilibrium phase transitions) have the added feature that these self-organized structures are generally in a dynamical equilibrium state, meaning they are sustained through the competition of growth and decay tendencies (as highlighted by the well-known fluctuation-dissipation theorem, proved mostly at close-to-equilibrium regimes but is also valid at far-from-equilibrium situations for self-organized dissipative structures). There is in general also a continuous flux of energy and entropy through the system to maintain the nonequilibrium fluctuation. The formation of self-organized dissipative structures in nonequilibrium systems often serves the important function of greatly accelerating the speed of

entropy evolution of the parent systems (Prigogine 1980)<sup>1</sup>.

The hierarchy of self-organization processes in a nonequilibrium system often leads to a series of effective singularities in the dynamics, which allow *emergent* new dynamics to form that cannot be *deductively* derived from the differential formulation one starts the analysis with. A synthetic approach uniting the various local aspects to achieve global self-consistency will need to be adopted. The correlations among the fluctuations of the individual degrees of freedom of the many-body system are shown to play a crucial constructive role at the juncture of nonequilibrium phase transitions.

Although the mechanism for the generation of new dynamics through so-called “spontaneous breaking of gauge symmetry” had been routinely proposed in high energy physics, it was mostly used in a model context, rather than derived from first principles in a self-consistent fashion. Quoting once again condensed matter physicist P.W. Anderson: “... the concept of broken symmetry has been borrowed by the elementary particle physicists, but their use of the term is strictly an analogy, whether a deep or a specious one remaining to be understood” (Anderson 1972). On the other hand, the fact that, as of now, there have been very few examples of self-organized dissipative systems being analysed from first principles (in Prigogine’s work, chemical clock was used as one prominent example) is partly due to the intrinsic complexities of such problems, i.e., the many degrees of freedom of the components, and the correlations among the components, which invalidate many basic assumptions underlying the usual kinetic theory approach for treating many-particle systems. One of the most important assumptions used in the derivation of the Boltzmann kinetic equation is the so-called “molecular chaos” assumption (see, e.g., Kreuzer [1981] for a detailed description of the BBGKY procedure for the derivation of the collisional Boltzmann equation), or the assumption that particle collisions are uncorrelated. This assumption is crucial to Boltzmann’s arriving at his famous H-theorem, or that entropy

---

<sup>1</sup>The transportation of entropy to its environment is the chief reason a dissipative structure can maintain a low or constant entropy state despite it being a very efficient engine at the local production of entropy. This aspect also resolves the paradox of how nature can generate complex biological entities such as human being as a result of nonequilibrium evolution, despite being governed by the second law of thermodynamics universally. The study of nonequilibrium dissipative structures tells us that entropy increasing evolution does not always mean the rush towards homogeneity everywhere, at least not for open, many degree-of-freedom, far-from-equilibrium systems.

never decreases in nonequilibrium processes. The inter-particle correlations, however, are the necessary ingredient for obtaining self-organized behavior, and their re-introduction into the study of nonequilibrium dynamics allows local-entropy-decreasing processes to be admitted into the analyses.

N-body simulations of self-gravitating systems, in our case the simulation of disk galaxies containing self-organized density wave patterns, offer a rare chance to observe at close range the modification of differential dynamics to arrive at new (i.e. emergent) meta-laws, thus offer clues to the common features of spontaneous symmetry breaking processes in many-degrees-of-freedom dynamics. In this case, an added advantage is that a parallel theoretical development has also been accomplished in the past few decades, which can serve as standards of comparison with the simulation results.

### *1.2. Secular Evolution of Galaxies in the Context of Nonequilibrium Phase Transition*

The striking coherence of spiral and bar patterns in disk galaxies has long captured our awe and fascination, but it was only since the advent of density wave theory (Lindblad 1963; Lin & Shu 1964; Kalnajs 1965) that these patterns were understood as propagating waves of over-density in differentially rotating galaxy disks<sup>2</sup>.

As the study of density waves in galaxies progressed over the past few decades, the propagating wave picture of the initial studies further evolved into a *modal* view, in which the oppositely-propagating trains of density wave in the radial direction superpose to form growing density wave *modes* (Lin & Lau 1979 and the references therein; Bertin et al. 1989a,b). In this formulation the so-called “grand-design” spirals and bars observed in nearby galaxies were regarded as spontaneously growing modes in a galactic resonant cavity whose properties are characterized by the axisymmetric distributions of disk-mass surface density, stellar and gaseous velocity dispersions, as well as the overall gravitational potential field (which include contributions not only from the disk mass, but also from the more spherically distributed luminous

---

<sup>2</sup>The publication of the first round of density wave papers followed shortly after the appearance of the first volume of “The Feynman Lectures on Physics” in which Feynman suggested to the freshman and sophomore physics students in his class: “Incidentally, if you are looking for a good problem, the exact details of how the arms are formed and what determines the shapes of these galaxies has not been worked out” (Feynman, Leighton, & Sands 1963).

and dark halos, as well as the galactic bulge), which together form the so-called “basic state” of the galactic disk, upon which the wave modes grow as unstable harmonic perturbations<sup>3</sup>.

During the early decades of density wave study, the basic state of the galactic disk was treated as a stationary background from which the unstable trains and modes of density waves were calculated to varying orders of approximation (according to the orderings of either the degree of non-linearity, or else the degree of locality in the successive WKBJ approximations). The prospect of the secular evolution of the mass distribution of the basic state itself was never seriously considered, apart from phenomenological inferences of the possible role of gas accretion (Kormendy 1979). As we know, gaseous mass in galaxies forms only a small percentage of the total disk mass, and the disk mass in most intermediate- and early-type galaxies was dominated by stellar mass. Therefore, a significant transformation of the Hubble type of a galaxy during its lifetime will necessarily involve the secular redistribution of the *stellar* mass, in conjunction with the redistribution of the gas mass.

The long-held view that the stellar disks of galaxies remain mostly unchanged throughout a galaxy’s lifetime is partly a result of the belief that stars behave “adiabatically” during their orbital motion, and do not dissipate their orbital energy when interacting with a stationary density wave except at the wave/particle resonances (Lynden-Bell & Kalnajs 1972) – a behavior summarized by the well-known “conservation of the Jacobi integral” of a single star’s orbit in the rotating frame of a stationary wave perturbation (Binney & Tremaine 2008). Another often-used phrase to describe this quasi-stability of the stellar orbit is the so-called “angular momentum barrier” to secular redistribution of stellar mass in a disk galaxy.

Observationally, there is growing evidence that galaxy morphology does evolve significantly throughout the cosmic history, in general following the trend from a disk-dominated late-Hubble-type to a bulge-dominated earlier-Hubble-type (Zhang 2003; Kormendy & Kennicutt 2004; as well as the references therein). Though galaxy mergers had previously been proposed as responsible for a large fraction of galaxy Hubble-type evolution, there are strong dynamical reasons why mergers cannot be responsible for most of the observed morphological evolution of disk galaxies (Zhang 2003, 2008; as well

---

<sup>3</sup>The “basic state” of the galactic disk is formally equivalent to the so-called “boundary condition” in an electromagnetic resonant cavity.

as the references therein). Boxy early-type disk galaxies, and especially the massive cD-type galaxies in the central regions of dense clusters, are the only prime candidates for the merger mechanism of disk-galaxy morphological evolution.

How then could stars in disk galaxies overcome the angular momentum barrier, break the constraint of the conservation of the Jacobi, and initiate significant redistribution of stellar mass during the lifetime of a galaxy? As it turned out, the answer had much to do with the dynamics of the self-organization process which formed the global density wave patterns in the first place, as well as with the theory of dissipative structures. Zhang (1996, 1998, 1999, hereafter Z96, Z98, Z99, respectively) showed that stars in galaxy disks possessing spontaneously-formed nonaxisymmetric density wave modes, such as spirals and bars, are able to display dissipation-like behavior just like their gaseous counterpart<sup>4</sup>, as long as the *collective mutual interactions* of the stars are taken into account. The conservation of the Jacobi integral for a single star's orbit is shown to be purely a consequence of having treated such an orbit as *passively* responding to an *applied* potential field, which ignored the *mutual interactions* of stars in a *self-sustained* density wave mode. The passive treatment does not incorporate the graininess effect of the spiral and bar potential which reflects the inherent correlations among the orbits of the stars (as well as gas clouds).

The detailed analyses of the workings of collective effects in spiral and barred galaxies were previously presented in Z96 and Z98. For a quick rehash, we look into the dynamical processes in galaxies from both the global and the local points of view – and ultimately, these two views need to give consistent results for spontaneously-formed and self-sustained density wave modes. Globally, modal formation is due to the fact a galaxy disk containing a density wave mode is generally more energetically favorable than the axisymmetric basic state from which the mode emerges. Therefore, the marginally axisymmetrically stable galactic disk, formed from the primordial collapse and dissipation of the gas clouds, is unstable to the formation

---

<sup>4</sup>In fact, as it turned out, gas also achieves efficient secular mass redistribution through *the same* gravitational torque mechanism as stars (Z98), since its participation in the interaction with the density wave is mostly through the scattering of clouds. The microscopic viscosity in the cloud medium can be shown to be entirely insignificant (compared to cloud scattering which has much greater mean-free-path) to the secular redistribution of gas mass in a galaxy disk environment.

of nonaxisymmetric spiral or bar modes. From another perspective, modal growth is due to the fact that the galactic resonant cavity for propagating density waves has a positive gain for the wave amplitude during each round trip of the wave-train propagation between the corotation circle and the inner galaxy. The wave amplification happens mostly near the corotation region through the so-called “over-reflection” of the outward propagating wave train to become an inward propagating wave train of higher amplitude, and the accompanying transmission of angular momentum across the corotation radius to a third wave branch which propagates to the outer disk to dissipate the energy and angular momentum to the environment<sup>5</sup>.

Figure 1 shows a schematic of the wave amplification process (Mark 1976; Toomre 1981). The over-reflection mechanism at corotation removes angular momentum from the waves inside corotation, and delivers it to outside corotation to be dissipated in the outer disk. Due to the change of sign of wave angular momentum density across the corotation radius, this angular momentum redistribution process through the wave propagation and over-reflection at corotation causes the wave branches both inside and outside corotation to grow indefinitely, if no nonlinear and dissipative mechanism are present to counter the growth tendency.

The *global* spontaneous growth tendency of the unstable mode in realistic galaxy disks is counter-acted by the *local* dissipation at the spiral (or bar) arm locations, since each time as disk material crosses the arm density wave crest during its circum-galactic rotation, it loses angular momentum to the wave potential field through the mediation of a collisionless shock (Z96), for matter inside the corotation radius. The sense of angular momentum transmission is reversed, i.e. from the wave to the disk matter, for the orbiting matter outside corotation. This angular momentum exchange between the wave and the basic state disk matter is of the correct sense both inside and outside corotation to lead to the damping of the growing wave amplitude (since the wave has negative angular momentum density with respect to the basic state, upon receiving angular momentum from the disk matter its amplitude

---

<sup>5</sup>Note that an idealized density wave mode rotates in the azimuthal direction with a fixed pattern speed, and since the galaxy disk itself possesses differential rotation, the disk matter rotates faster than the density wave inside the corotation radius, and thus overtakes the density wave; and vice versa outside corotation. *The wave thus have negative angular momentum density inside corotation relative to the basic state, and positive angular momentum density relative to the basic state outside corotation.*

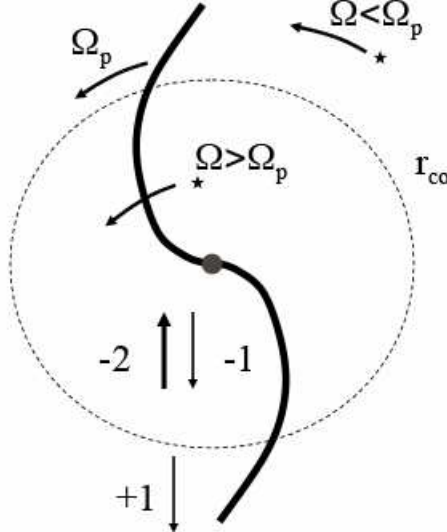


Figure 1: Schematic of the wave propagation and amplification in the galactic resonant cavity to form infinitely-growing density wave modes. The symbols  $\Omega$  and  $\Omega_p$  denote the galaxy (or disk matter) circular/angular speed and density wave pattern speed, respectively. Inside the corotation radius the stars overtake the wave during their circulation around the galaxy, and vice versa outside corotation. Here the circle with radius  $r_{co}$  is the corotation circle. The numbers next to the arrows indicate the normalized amount of wave angular momentum relative to the basic state for the respective segment of the outward propagating (incoming) and inward propagating (over-reflected) wave trains inside corotation, as well as the outward propagating (transmitted) wave train outside the corotation radius. Note that the over-reflection process conserves angular momentum, which we can check by summing the two numbers after the over-reflection process (-2 and 1) and compare the result with the number before the over-reflection process (-1). The feedback loop is completed by an inner Q-barrier (usually identified with the galactic bulge region), where the inward-propagating wave train gets turned around to become the outward propagating wave train for the next cycle of over-reflection at corotation. This illustration is for the milder version of the over-reflection mechanism WASER (Mark 1976). For the SWING mechanism (Toomre 1981), the over-reflection factor can be significantly bigger than the factor of 2 illustrated here. The SWING and WASER mechanisms differ by whether the incoming wave train towards corotation is that of the leading or the trailing type, respectively, produced in turn by either the inward-propagating trailing wave tunneling through the central region of the galaxy when no Q-barrier exists, and emerging as a leading wave; or else by the inward-propagating trailing wave being reflected by the Q-barrier when one exists, which produces an outward-propagating trailing wave. The SWING mechanism tends to produce bar-like modes, and the WASER mechanism spiral modes.

decreases. Similarly the sense of angular momentum exchange, and the sign of angular momentum density of the wave, outside corotation lead to the damping of the wave outside corotation as well). Eventually, at sufficiently nonlinear amplitude, the wave mode achieves a quasi-steady amplitude and the galaxy settles into a dynamical equilibrium state (Z98).

This equilibrium is called *dynamical* because it is maintained through the competition of opposing tendencies of wave-mode growth and damping, and is maintained also at the expense of dissipative secular evolution of the basic state mass distribution: the disk matter inside corotation, upon giving angular momentum to the wave at each arm crossing, spirals slightly inward; and the matter outside corotation spirals slightly outward after each arm crossing. The dissipative secular evolution of the basic state allows the accomplishment of another mission of dissipative structures, that of enhanced entropy production and export by these structures. As is well known the direction of entropy evolution for a self-gravitating system is towards ever increasing central concentration, together with the buildup of an extended outer envelope (Antonov 1962; Lynden-Bell & Wood 1968). This direction of entropy evolution for self-gravitating systems is the same as that of the galaxy morphological evolution along the Hubble sequence from the late to the early Hubble types.

The angular momentum exchange between the wave and the basic state is made possible through a collisionless gravitational shock at the density wave crest (Z96), similar in nature to the well-known plasma collisionless shocks (Balogh & Treumann 2013 and the references therein). The correlated interactions of the orbiting stars (which can also be viewed as mediated by the correlation between the grainy potential field of the wave and the individual particles' motion), scatter the stars mildly each time they cross an arm, to allow just the right amount of angular momentum exchange between that contributing to the stellar orbital motion and that contributing the wave motion, in order to counter the growth tendency of the wave mode as well as to initiate the secular orbital decay (inside corotation) or increase (outside corotation), at the quasi-steady state of the wave mode.

The meeting point between the local and global points of view is the global self-consistency requirement, i.e., since the dissipative density wave mode is self-sustaining and self-limiting, the combined effects of various dynamical processes on the wave and the basic state should be globally balanced and quasi-steady. The fact that this global self-consistency is achievable in galaxies is due both to the long-range nature of gravitational interaction, as

well as to the dependence of wave amplification and damping efficiencies on the nonlinearity of the density wave pattern (Z96, Z98).

The long-range nature of gravitational interaction (as manifested through the form of the Poisson integral) means that the density and its associated potential field do not always coincide in space. In the case of a skewed density wave mode, this nonlocality of potential manifests as a characteristic radial distribution of the azimuthal potential-density phase shift. As shown schematically in Figure 2, the radial distribution of the potential-density phase shift, for an unstable spiral or bar mode, is such that the spiral perturbation potential lags the perturbation density inside the corotation, and vice versa outside the corotation. This characteristic distribution of the potential-density phase shift is admitted by both the Poisson integral and by the equations-of-motion for the particular set of solutions of disk-mass and particle-velocity distributions that support a spontaneously-formed density wave mode (Z96, see especially the Appendices there).

At the quasi-steady state of the wave mode, the characteristic phase shift distribution represented in Figure 2 implies a secular torque action by the wave potential on the basic state disk matter, which leads to secular angular momentum exchange between the wave and the basic state both inside and outside corotation. This secular torque action can be shown to be responsible both for the spontaneous emergence of the wave mode in the linear regime, as well as for the maintenance of the mode to a quasi-steady amplitude at the expense of dissipative basic state evolution (Z98).

The characteristic phase shift distribution represented in Figure 2 is both the symptom, as well as the driving dynamical mechanism, for the underlying secular dissipative process. For example, the existence of this phase shift is one of reasons that collisionless shock at the spiral arm crossing can form to initiate dissipation, since the streaming disk matter, while marginally gravitationally stable before arm crossing, experiences added compression due to the nonlocal gravitational potential contributed by the rest of the disk matter, which drives the streaming matter below their instability threshold and thus enabling the collisionless shock (Z96). On the other hand, secular angular momentum exchange between the density wave potential and the underlying disk mass distribution (as needed for wave damping and basic state evolution) necessarily leads to an azimuthal potential-density phase shift, a fact already hinted at in Kalnajs (1972), though there it was the interaction between a non-self-consistent *gaseous* density wave and a driving *stellar* potential wave that was the subject of study (i.e., the exploration of

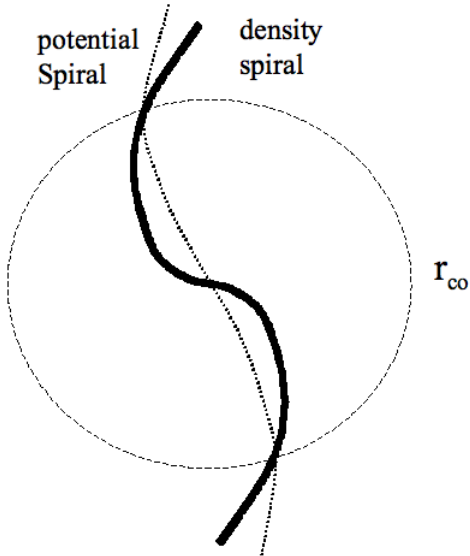


Figure 2: Schematic of the radial distribution of the azimuthal potential-density phase shift for a self-sustained density wave mode in a galaxy disk. The solid line indicates the locus of the peaks of the density spiral, and the dotted line indicates the locus of the troughs of the potential spiral. The circle indicates the corotation circle where the density wave pattern speed and the basic state matter's circular speed are the same. It is also where the potential-density phase shift is zero for a spontaneously formed density wave mode (Z96; Zhang & Buta [2007]; Buta & Zhang [2009]).

using gaseous wave as a candidate for the damping of stellar wave), rather than the self-interaction of spontaneously-formed density wave mode.

As valid for all collective or cooperative effects, here we witness in spiral and barred galaxies a seeming miracle, of all the diverse components of the system cooperate to accomplish a central goal: to accelerate the entropy evolution of the nonequilibrium system. These coordinated interactions are accomplished through a global instability pattern (here the density wave modal pattern), which spontaneously emerge in far-from-equilibrium systems. Their longevity is one of the reasons we observe them (in nature there are no lack of systems that self-destruct not long after emergence, and thus have short lifetime. Even for spiral galaxies themselves there are constant appearance of transient noise, as well as slow-growing modal components that die out in the competition with the most unstable modes – which is one reason why dissipation is so important in the operation of these systems: In sufficiently nonlinear regime all fluctuations receive damping, but only the dominant modal components receive sufficient amplification to offset the damping). So the seeming miracle of cooperation among the components of self-organized systems is partly a result of a natural selection process, though

this selection happens on much shorter timescale (as fraction of the lifetime of a single dynamical system) than biological natural selection, which happens through many generations of individual members. We can instead call this rapid natural selection process in self-organized systems a “winner takes all” process, i.e., in the case of a galaxy, the dominant mode rapidly solicits all resources of a disk galaxy’s mass distribution to modal activity, and after a few dynamical timescales little is left for the slower-growing modes and noise, which all receive additional damping through the local dissipation mechanism at the density wave crest. Other examples of such dissipative structures in nature include the hexagonal convection cells in the well-known Benard problem of atmospheric heat flow, as well as human beings who are capable of the most efficient entropy production and export. In some sense, dissipative structures are the tools nature manufactures to accomplish the task of accelerated evolution in nonequilibrium systems.

### *1.3. N-body Simulations of The Secular Evolution of Disk Galaxies*

N-body simulation of self-gravitating systems has had a long history (see, for example, Sellwood [1987] and Hockney & Eastwood [1988] for reviews of the early decades’ work). For the modeling of disk galaxies, N-body simulations were often carried out in a two-dimensional (2D) configuration, emulating the thin disks in observed galaxies, with the spherical bulge and halo modeled as inert and time-independent. To save computation time, 2D galaxy-disk simulations often employed a particle-mesh approach, with the force calculation performed on a regularly-spaced mesh and then interpolated to the individual disk particles, rather than being performed directly.

After assigning (usually constant) mass to the simulation particles (each has many solar masses depending on the total number of particles used in a given simulation and the total disk mass), with the particles distributed according to a given galaxy’s disk surface density, the particle masses are further grouped/assigned onto the corresponding grid points. Grid potential (or force) are calculated using the Poisson integral, aided by Fourier transform techniques whenever possible, and then interpolated back onto individual super-particles (usually through the same algorithm as the mass assignment algorithm in order to conserve momentum). These forces are used to calculate accelerations on the individual particles, and the particle trajectories are advanced through a standard finite difference algorithm such as leap frog. Then the cycle starts anew. Time step and spatial grid spacings are selected to ensure stability and accuracy, and special treatments at the

inner and outer boundaries of the disks are needed to take care of in-spilled and out-spilled particles leaving the computation grid.

Earlier N-body simulations of disk galaxies containing density wave patterns focused on the emergence phase of the patterns, and checked the growth rates against linear density wave theory predictions, and derived pattern speeds and other related density wave parameters (Sellwood 1987 and the references therein). Donner & Thomasson (1994) first explored the longevity of density wave modes in N-body disk simulations. They found initial evidence of the mass inflow/outflow behavior for stars inside and outside of corotation, respectively, but did not attribute a dynamical mechanism to it.

Starting from her Ph.D. dissertation work (Zhang 1992), the current author had carried out a systematic study of the dynamical mechanisms underlying the secular morphological evolution of disk galaxies enabled by the self-organized density wave modes. Building on the numerical algorithms for N-body simulation of Thomasson (1989), which was a direct decendent of polar-grid code originally developed by Miller (1976), Z96 & Z98 explored the signature of collisionless shock in spiral galaxies, the potential-density phase shift distribution, as well as the secular evolution of the basic state mass distribution in the simulated galactic disks, and compared these with the theoretical predictions.

Despite the confirmation of theoretically-derived mass flow rates in the accompanying N-body simulations (Z98), which established the viability of the analytical approach, the simulated mass flow rates were found to be small, far from being adequate to lead to significant morphological transformation of a galaxy within a Hubble time. This small mass flow rate was traced back to the small amplitudes of the spiral patterns formed in the simulations, which are far short of the extremely-nonlinear wave amplitudes observed in physical galaxies. This feature of the small wave amplitude applies to all the disk galaxy simulations performed in the past few decades, and its cause was barely addressed.

In order to circumvent the difficulty with simulations, Zhang & Buta (2007, 2015) used near-and-mid-infrared images of galaxies and applied the analytical mass flow rate equation of Z96 & Z98 (see also equation 8 in Appendix A of the current paper) directly to the derived mass surface density of physical galaxies. In these studies, it was found that mass flow rates from a few  $M_{\odot}$  per year to over one hundred  $M_{\odot}$  per year were typical, depending the density wave amplitudes and pitch angles of galaxies. These derived mass flow rates for physical galaxies far exceeded those obtained from past N-body

simulations, mainly as a result of the fact that mass flow rate is proportional to the wave amplitude squared (Appendix A), and the amplitudes in physical galaxies are oftentimes a factor of 3-10 times higher than those obtained in N-body simulations, implying a difference in mass flow rates of a factor of 10 - 100 between physical and previously-simulated galaxies.

Given the importance of understanding secular evolution processes in physical galaxies, one could not help but wonder what exactly were the factors that prohibited the simulated disk galaxies from achieving the range of density wave amplitudes and the level of mass inflow rates in observed galaxies. It is to this question that the current paper addresses. We show that an artificial parameter inserted into the numerical equation for calculating gravitational potential, i.e. the so-called *softening parameter*, underlies much of the discrepancy between the simulated and observed wave amplitudes. Softening was introduced to represent both the finite thickness effect of realistic galaxy disks in 2D simulations, and to restrain the artificial relaxation effect that is more pronounced in simulated disks which have a much smaller number of particles compared to observed galaxies. When properly chosen, it was found in the past that the exact values of softening parameter does not impact significantly the morphology of the simulated density wave patterns. On the other hand, as we will show in this paper, when our goal is to model the quantitative characteristics of the self-organized density wave modes, especially the nonlinear equilibrium amplitude of the quasi-steady wave modes which in turn determines the rate of the secular evolution of the basic state mass distribution, the role of softening turns out to be more subtle, due to the fact that the spontaneously formed modes are stabilized through the dynamical balancing act of global amplification and local dissipation. Both the modal amplification process (which is sensitively dependent on the self-gravity of the disk, especially near the corotation region) and the local dissipation of the wave (through the collisionless shock enabled by the mutual interactions of local matter within the arm instability region) depend on the exact form of the force law, or the departure of this law from the original Newtonian form as a result of softening. The net effect is that smaller softening leads to equilibrium wave-mode amplitude and the resulting secular mass flow rates much closer to what we had measured from observed galaxies (Zhang & Buta 2007; 2015).

Besides impacting the equilibrium wave amplitude, we show that small softening leads to easier attainment of quasi-steady modes. The wave patterns obtained in small softening runs, though locally often appearing more

noisy, are in fact globally closer to pure modal forms, as borne out from power spectrum analyses. Even the noisier local mass distribution itself in the small softening simulations is in fact closer to how observed galaxy mass is really distributed, i.e., an average galaxy disk is often populated by stellar clusters, globular clusters, giant molecular cloud complexes, and other spiral arm inhomogeneities. In the face of all the inhomogeneities in mass distribution, the grand-design density wave modal patterns are nonetheless often obtained among observed galaxies. It is thus reassuring that the robustness of observed density wave modes<sup>6</sup> can be reproduced in the simulations using small softening parameters. This shows that self-organized nonequilibrium patterns possess so-called “asymptotic stability” and are unaffected by the incidentals of the noisy background. If anything, the noisy mass distribution provides the necessary initial seeds for the rapid spontaneous growth of the instability pattern.

## 2. THE EFFECTS OF SOFTENING IN N-BODY SIMULATIONS OF DISK GALAXIES

In this section, we motivate the study in the main body of this paper (sections §3-§4) by giving the historic context and rationales for the introduction of the softening parameter in N-body simulations of disk galaxies, as well as the potential limitations when softening is used in modeling the long-term (secular) evolution behavior of disk galaxies containing self-organized density wave patterns. We also present a first set of simulations showing the dependence of the rate of disk mass redistribution on the choice of the softening parameter, as well as on other parameters of the simulation.

### 2.1. *Background*

In essentially all of the gravitational N-body simulations of galaxies, a so-called softening parameter is used to control the artificial relaxation effects due to the smaller number of particles used in these simulations compared to that in physical galaxies. The softened force law can take various analytical forms. In the often employed Plummer-sphere softening scheme, the gravitational potential due to a point mass  $m$  at a distance  $r$  is calculated as

---

<sup>6</sup>See also Zhang & Buta (2015). In the cases of M51 and NGC 3627 analyzed there, the intrinsic modal features of these galaxies were shown to be preserved even after strong tidal interactions with companion galaxies.

$$\Phi(r) = \frac{-Gm}{\sqrt{(r^2 + a_{soft}^2)}} \quad (1)$$

where  $a_{soft}$  is the softening parameter, and G is the gravitational constant. A choice of  $a_{soft} = 0$  corresponds to the original Newtonian force law. A finite softening parameter reduces the amount of unrealistic close encounters which occur more frequently for small N (N here denotes the number of particles used in N-body simulations) systems, and thus reduces the level of artificial relaxation in such systems. Furthermore, in the particle-mesh approach commonly adopted in simulating disk galaxies, the mesh size itself provides additional softening effect. The hope is that a *collisionless* configuration would result from a well-matched N and an *effective* softening parameter which takes into account both particle and grid softening effects. In the context of 2D disk galaxy simulations, both particle and mesh softening also emulate the realistic physical configuration of finite disk thickness. 2D simulation incorporating softening has been shown to be able to model the realistic macroscopic properties of disk galaxies containing density wave patterns with  $10^3 - 10^7$  less number of particles than that present in physical galaxies.

One of the rationales for introducing the softening parameter is to achieve an effectively collisionless environment for the duration of the simulation run, so that only long-range interactions determine the formation of density wave patterns in their parent disks. However, with the realization that galaxies which possess global density wave modes *always* involve partly-local collective dissipation processes, one soon faces the fact that it is impossible to completely avoid collision-like behavior in the simulation of unstable density wave modes, no matter how large a particle number N is used (whether in real galaxies or in simulations): After all, collective effects in these systems *depend* on the near-collision or small-angle scattering of particles in the global instabilities (i.e. density wave modes) to set up long-range correlations, in order to achieve self-organization and to induce secular evolution of the basic state of the disk (Z96). In some sense, these galactic systems are in a *forced relaxation configuration*, with the forcing accomplished by the density wave collisionless shocks. The *effective* local instability parameter  $Q_{eff}$  in the spiral arms is thus always less than one to enable interparticle correlation. *A true collisionless configuration will never be able to support self-organization behavior.*

The custom choice of large softening in the past N-body simulations of disk galaxies, however, reduces the very interparticle interaction that is the backbone support of collective effects, and thus can be responsible for reducing density wave amplitudes in simulated galaxies, as had already been noticed early on (Sellwood 1987). Despite perhaps subconsciously knowing the correlation between the choice of softening parameter and the simulated wave amplitude by some researchers, the practice of using large softening (i.e. using a value comparable to the smallest grid size) continued almost universally, partly because these earlier N-body simulations were mainly interested in obtaining a comparable appearance of density wave morphology as that in observed galaxies. They are not geared towards the study of secular evolution effects induced by the collective density wave modes, which will require the accurate simulation both of the morphology as well as the amplitude of these density wave modes.

In a series of papers, Romeo (1994, 1997, 1998) conducted systematic studies of softening on the quality of N-body simulations, and advocated against using large particle softening in N-body simulation. Furthermore, he pointed out that “A delicate aspect of the relaxation problem that has not been considered in the previous discussion concerns the effects of collective interactions between particles and self-consistent fluctuations on the dynamical evolution of the system (e.g., Romeo 1990 and the references therein; Weinberg 1993; Z96). A thorough treatment of collective effects would demand titanic efforts even in simpler models (cf. Weinberg 1993)” (Romeo 1997)<sup>7</sup>.

It is indeed to these aspects of the collective interactions of particles, as well as the self-consistent fluctuations in galaxy dynamics that the work of Z96, Z98, Z99 and Zhang & Buta (2007, 2015) were devoted. The current paper is a continuation of this line of work, focusing in particular on factors that produced the difference between the simulated and observed galaxy characteristics. We highlight below that overly-softened gravity modifies the Newtonian force into a more sluggishly-interacting one that hampers the proper operation of collective effects. This might not be a serious concern if one’s interest is in obtaining a coherent modal morphology that mimics

---

<sup>7</sup>Weinberg (1993) treated the effects of collective interaction on the relaxation processes in symmetric and periodic systems. These systems did not contain self-organized density wave patterns, thus are passive systems.

the observed galaxy morphology (e.g. Donner & Thomasson 1994, hereafter DT94). However, it can be detrimental to the determination of realistic secular mass flow rates that are relevant to physical galaxies.

## 2.2. Softening and Its Effect on Secular Mass Flow Rates

In Figure 3, we present a set of N-body simulations of the density-wave-induced secular evolution of disk galaxy mass distribution, using the basic state specification similar to that first explored in DT94, and subsequently used for the study of collective effects and secular evolution in Z96, Z98, Z99. The details of the basic state properties (mass distribution, rotation curve, and velocity dispersion distribution) are given in Appendix B of the current paper, while the dynamical mechanism which induced the secular evolution of the basic state mass distribution is summarized in Appendix A. In the current section we will only present the signatures of radial mass flow, while leaving the quantitative comparison to previously derived analytical mass flow rates to §3 (see especially §3.6).

All the simulations in the current paper are performed in a two-dimension (2D) configuration, using a particle-mesh approach on a polar grid (Miller 1976). The polar codes used in the current paper were written by the author based on algorithms described in Thomasson (1989). These codes have been used extensively in the development of the secular evolution theory in Z96, Z98, Z99, and many results were cross-checked with that presented in DT94. More details of the simulation grid and simulation procedure are given in Appendix C of the current paper.  $N=1$  million active disk particles are used in this first set of simulations presented in Figure 3.

The polar grid used has 220 radial rings and 256 azimuthal spokes. The distribution of the radial spacing is exponential, and the azimuthal spokes have equal spacings. The time step is chosen such that 1256 time steps represent one rotation period at  $r=20$ . The gravitational constant  $G$  is renormalized to accommodate this choice of spatial and temporal normalization and resolution (see further details in Appendix C). *These grid and time step resolutions are used in the rest of the simulations presented in this paper as well (except for the grid-resolution tests presented in Appendix D3), and only the particle numbers  $N$  and the softening parameters  $a_{\text{soft}}$  are changed and will be noted in each case.*

Incidentally, if one does not feel comfortable with the normalized units used here (which was originally introduced in Thomasson [1989] and Donner & Thomasson [1994]), one can attach a “kpc” to the normalized length unit,

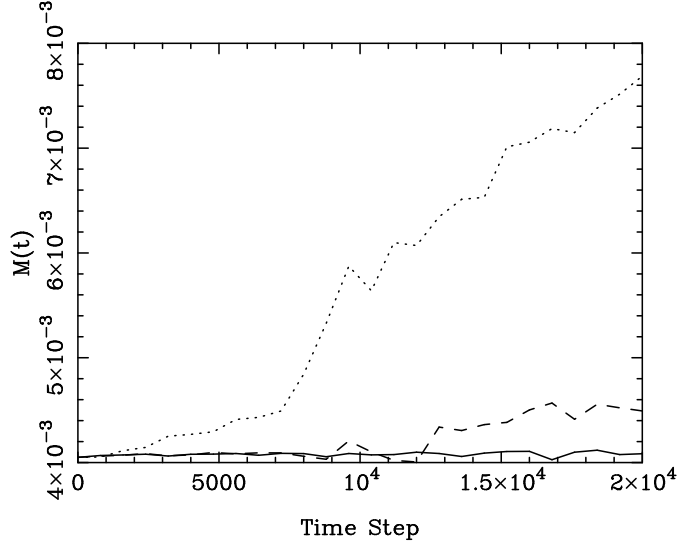


Figure 3: Evolution of enclosed disk mass within central  $r=3.5$  radius of a set of 2D N-body simulations with different softening parameter  $a_{soft}$ . Solid:  $a_{soft} = 1.5$ , Dashed:  $a_{soft} = 0.75$ , Dotted:  $a_{soft} = 0.25$ . N=1 million particles are used to represent the active disk.

a “ $10^{11} M_\odot$ ” to the normalized mass unit, and can scale the time steps to the unit of 1256 steps for one rotation period at  $r=20$ , for the results presented in the main body of the paper (and half as many steps per rotation period for results presented in Appendix D3 for a coarser grid and a larger effective time step choice) to aid in the intuitive comparison with physical galaxy properties.

The curves in Figure 3 are for the evolution of enclosed disk mass within the central  $r = 3.5$  region (in the scale of this disk which has corotation radius in the approximate range of 18-30 depending on the softening length used and on the epoch of secular evolution, the disk region within  $r = 3.5$  corresponds roughly to the central bulge region). The three curves, from bottom to top, correspond to softening parameter values of 1.5 (as used in DT94 and Z98), 0.75, and 0.25 in the unit of the radius of the innermost grid ring (or inner computation boundary) size of 1. As can be seen from the figure, the choice of softening of 1.5 (which is a common choice by N-body simulators) produced a barely noticeable mass inflow in the duration of the simulation run, which results in a central mass growth of 6.5% over roughly 25 rotation periods, which is obviously quite inadequate in transforming galaxy morphology in a Hubble time. Gradually reducing softening as shown in Figure 3 is seen to systematically increase the mass inflow rate.

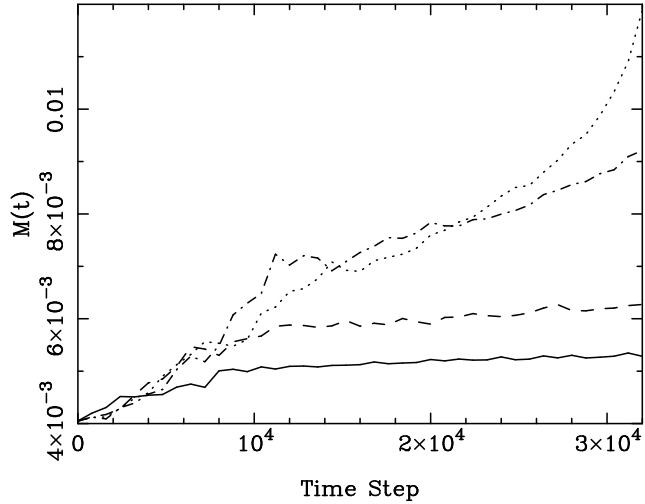


Figure 4: Enclosed mass within central  $r=3.5$  of the N-body disk for runs with different number  $N$  of active disk particles, and a constant  $a_{soft} = 0.1$ . Solid:  $N=1$  million particles. Dashed:  $N=10$  million particles. Dotted:  $N=20$  million particles. Dash-Dotted:  $N=40$  million particles.

The price one pays for reduced softening in small- $N$  simulations is the increase in relaxation (heating) rate and the formation of local instability clumps (see later among the morphological plots in §3.1). To compensate for the unrealistic degree of relaxation in small-softening simulations, one needs to use a correspondingly increased number of particles. How much the particle number needs to be increased for a given choice of softening parameter can in fact be obtained empirically. For 2D simulations, we found that for a factor of  $f$  reduction in the particle softening parameter, an increase of  $f^2$  is needed in the number of particles to keep the heating effect in check. This scaling behavior had also been found in previous studies by other authors (e.g. Thomasson, Donner & Elmegreen 1991).

In Figure 4, we show a set of simulations with changing particle numbers while holding the softening parameter  $a_{soft} = 0.1$  (the smallest softening choice that will be explored in the current paper). For the small particle-number runs, the rapid mass inflow is seen to saturate at an earlier time step, which corresponds to the time (as revealed from the morphological plots) when the spiral activity is damped by the excess heating due to the insufficient number of particles, especially in the outer disk region where the surface density is low, the grid size is large, and the particle numbers are small. For large particle number runs, the rapid mass inflow is seen to remain

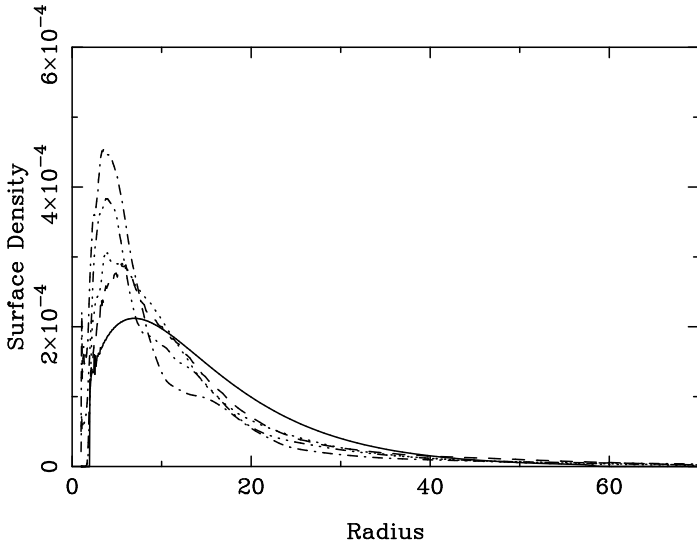


Figure 5: Basic state surface densities at the beginning (solid), and the end of four N-Body runs with different number of particles. Dashed: end surface density for 1 million particles. Dotted: end surface density for 10 million particles. Dash-and-Single-Dotted: end surface density for 20 million particles. Dash-and-Triple-Dotted: end surface density for 40 million particles.  $a_{soft} = 0.1$

at a constant rate all the way until the end of the run, which corresponds to 25 galactic rotations at the reference radius  $r=20$ . This indicates that the increased particle number (20 million/100,000=200) is adequate in offsetting the reduction in softening ( $f=1.5/0.1=15$ ), conforming to the  $f^2$  scaling law mentioned in the previous paragraph.

Furthermore, we note that the maximum mass inflow rate observed here (from the near constant slope of the large particle-number runs with  $a_{soft} = 0.1$ ) corresponds to about 60% increase in enclosed mass within  $r=3.5$  (the bulge region) over 10 rotation periods, or roughly 1/5 of a Hubble type. This level of mass accretion is more than sufficient to transform the Hubble type of a galaxy by several stages in a Hubble time, consistent with the level of mass flow rates derived for physical galaxies (Zhang & Buta 2007, 2015).

In Figure 5, we show the disk surface density at the beginning of the run, and at the end of the four runs with different numbers of particles (as presented in Figure 4, but here with different line styles from Figure 4 for each case due to the need to represent the “before” surface density). It can be seen that the large mass inflow of the large-particle-number runs indeed builds a more substantial bulge. However, the 20 million particle run in fact produced more substantial bulge-building than the 40 million particle run.

This is consistent with the trend observed in Figure 4, where it is seen that the 40 million particle run has somewhat reduced mass inflow rate near the end of the run. This saturation of the mass flow rate at a specific level of particle number matched to the decrease of softening length is reassuring since we expect the collective effects to be relatively independent of particle number once the excess relaxation effect is held under control by the use of sufficient number of simulation particles.

### 3. FOUR SETS OF VARIABLE-SOFTENING N-BODY RUNS

The initial tests of the last section show that by significantly decreasing the amount of particle softening, and simultaneously increasing both the number of simulation particles used as well as the degree of grid resolution, we can achieve increased radial mass flow rates to levels comparable to that needed for a significant change of galaxy morphological types over a Hubble time, as indicated in observational studies (Zhang & Buta 2007, 2015).

A natural question arrives as to whether this observed increase in radial mass flow rate is a true physical effect, or else is a numerical artifact due to noise brought about by the small softening and the corresponding increased collisional relaxation. To answer this question, in this section we present detailed correlations of density wave modal characteristics and the observed mass flow behavior in the N-body simulations. Softening will be shown to change the equilibrium amplitude of the modes formed, but it hardly changes the *level of agreement* between the mass flow rate *predicted* using the modal parameters found in the simulations, and the corresponding mass flow rate *measured* in the same simulations (i.e. smaller equilibrium wave amplitudes are found to correspond to smaller measured mass flow rates, given precisely by the theoretical predictions using the corresponding wave amplitudes).

In what follows, we will first establish the modal nature of the density wave patterns formed from originally featureless (axisymmetric) basic state of the galactic disk. After presenting the modal characteristics, we will go on to demonstrate the presence of the potential-density phase shift distribution, which leads to the secular torque interaction between the basic state mass distribution and the wave-mode potential field. This torque interaction leads to the angular momentum exchange between the basic state and the density wave, which further leads to the radial mass flow behavior. We demonstrate that both the qualitative and quantitative mass flow behavior observed in these simulations are consistent solely with the mode/basic-state interaction

picture, and are inconsistent with either the transient-wave- or noise-induced mass flow behavior.

Four sets of 2D N-body simulations are performed utilizing the same polar grid (220 radial grid cells, 256 azimuthal grid cells), the same number of particles (20 million), the same duration of simulation run (32768 steps, corresponding to roughly 25 galactic rotation periods at radius 20), and the same time resolution of 1256 time steps per galaxy rotation period time at  $r=20$ , but with the particle softening parameter having the values of  $a_{soft} = 1.5, 0.75, 0.25, 0.1$ , respectively, in the Plummer softening scheme (equation 1).

All the runs have the same basic state specification as that of Z98 (see also Appendix B of the current paper), which was also the basic state used in the previous section (§2). This basic state specification allows the setup of a galactic resonant cavity between the inner bulge region and the corotation radius in the mid-disk, and thus the formation of unstable density wave mode. The resulting corotation radius range from  $r_{co} \approx 28$  (for  $a_{soft} = 1.5$ ) to  $r_{co} \approx 23$  (for  $a_{soft} = 0.1$ ) at the initial emergence stage of the mode, and the corotation radius tends to decrease in the late stages as the secular mass inflow leads to a more centrally concentrated mass distribution.

### 3.1. Morphological Evolution

In Figure 6 to Figure 9, we present the morphological evolution of the density wave pattern with basic state and numerical grid specifications given in Appendix B,C, and with particle softening parameter  $a_{soft} = 1.5, 0.75, 0.25$  and  $0.1$ , respectively. The initial disk mass assignment is an axisymmetric modified exponential disk, and the rotation curve is nearly constant at a value  $v_c \approx 0.1$  in the normalized unit. The velocity dispersion assignment corresponds to the instability parameter  $Q_T \approx 1$  across the disk.

A coherent spiral-bar pattern spontaneously emerges from the originally featureless disk in each case. The morphology of the  $m=2$  (two-armed) dominant mode will be shown later in Figure 14, during its initial emergence phase. The mode in fact emerges at progressively earlier time steps as softening decreases, this will be shown more clearly later during detailed analyses. This is mainly due to the larger seed of noise present for modal amplification in the smaller softening cases.

The patterns in various cases contain other contaminants besides the  $m=2$  mode, for example the  $a_{soft} = 1.5$  case has some  $m=3$  component, and the

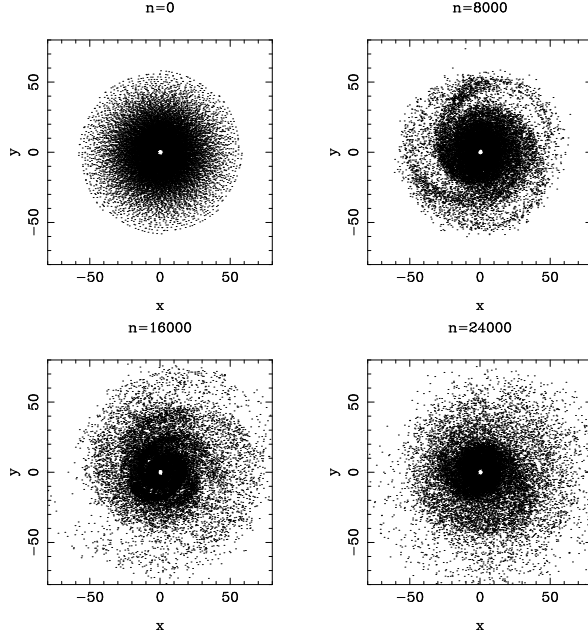


Figure 6: N-body morphology of a spiral/bar mode at different time steps. The rotation period at  $r=20$  is about 1256 steps. The softening parameter is  $a_{soft} = 1.5$ .

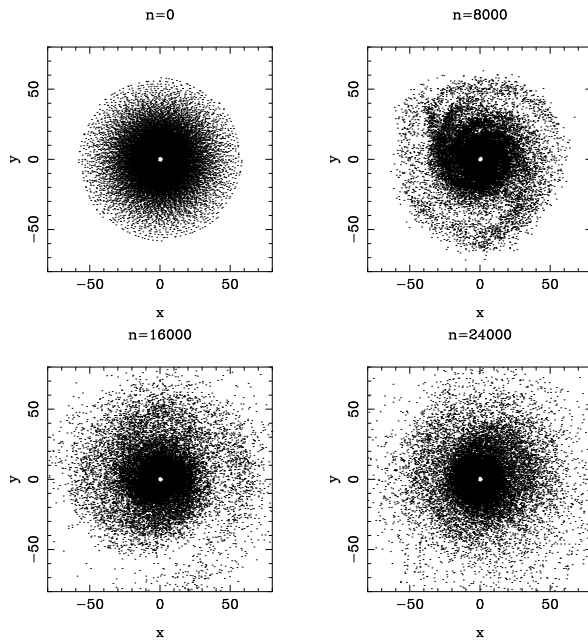


Figure 7: N-body morphology of a spiral/bar mode at different time steps. The rotation period at  $r=20$  is about 1256 steps. The softening parameter is  $a_{soft} = 0.75$ .

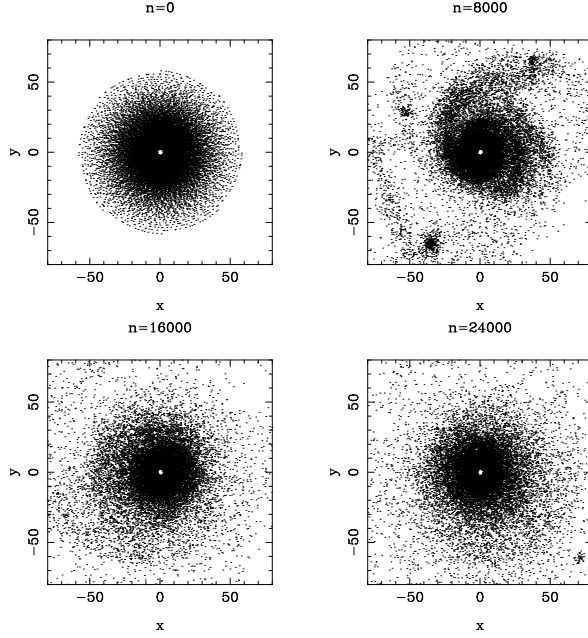


Figure 8: N-body morphology of a spiral/bar mode at different time steps. The rotation period at  $r=20$  is about 1256 steps. The softening parameter is  $a_{soft} = 0.25$ .

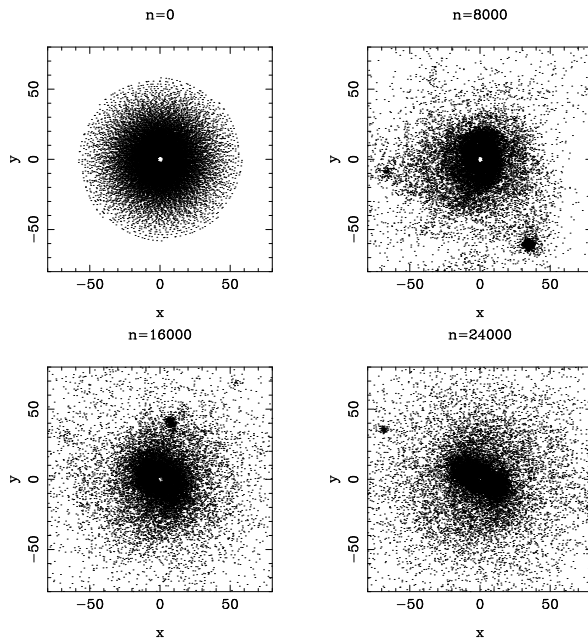


Figure 9: N-body morphology of a spiral/bar mode at different time steps. The rotation period at  $r=20$  is about 1256 steps. The softening parameter is  $a_{soft} = 0.1$ .

two small-softening cases ( $a_{soft} = 0.25, a_{soft} = 0.1$ ) are seen to have local instability clumps formed in the outer region of the simulation disk. The small softening cases also tend to have higher heating effect which submerges the nonlinear pattern within noise at the later stages of the simulation, though the underlying  $m=2$  mode can be shown to be persistently present in every case, for the entire duration of the simulation run (corresponding to 25 rotation periods at radius 20).

In the small softening case of  $a_{soft} = 0.1$ , the pattern is seen to have evolved from a spiral-like morphology in the early stage of the simulation to a bar-like morphology in the later stage, partly due to the rapid mass inflow in this small softening case. The increased central concentration of mass then favors a bar mode.

### 3.2. Phase Evolution

In Figure 10, we plot the time evolution of the azimuthal phase of the  $m=2$  (two-armed) perturbation-potential component from the above four runs, at a series of radii across the simulation disk.

The first thing we notice from this plot is the coherent, approximately linear, evolution of the phase at the various radial locations, for all softening choices, indicating that the patterns involved are rotating at nearly constant angular speed at each radius (though the pattern speed may change across the different radii, indicating the winding up of the pattern, especially for inner galaxy disk, and for large softening cases). This shows that the patterns that spontaneously emerged are likely to be unstable *modes* of the disk rather than random transient waves, with the latter not expected to have a coherent phase evolution over the lifetime of a galaxy.

Furthermore, we observe that while the phase evolution curves for the large softening runs diverge at the different radial locations, indicating a change of pattern speed for the different portions of the spiral arms (or the wrapping up of the pattern with time), the run with the smallest softening length ( $a_{soft} = 0.1$  case) shows an extremely constant pattern speed between  $r=10$  and  $r=30$  (i.e. between the inner Lindblad resonance and slightly beyond corotation radius). As a matter of fact, two of the 6 curves nearly overlap (that is why there appears to be only 5 curves).

Note also that in all cases the more rapid phase advance between  $r=5$  and  $r=10$  locations is likely to be due to a nuclear pattern with a separate pattern speed, since the outer main pattern has its inner Lindblad resonance at around  $r=10$ .

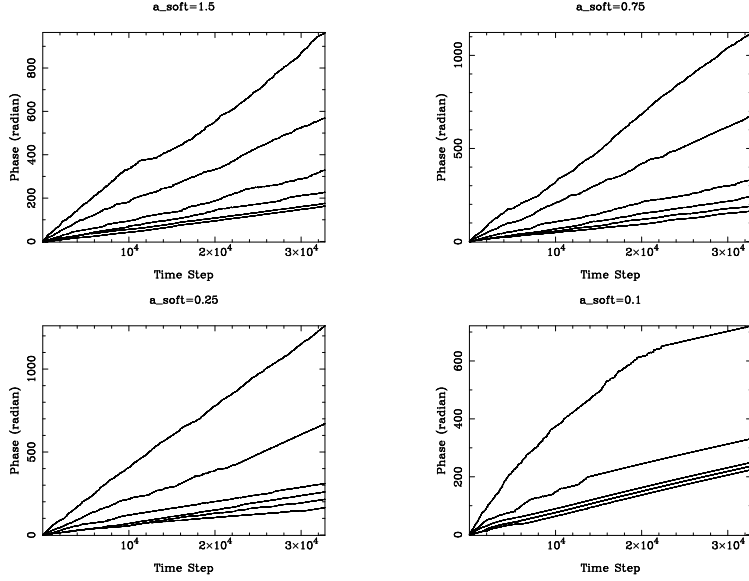


Figure 10: Phase evolution of the  $m=2$  potential at radial locations (from top to bottom)  $r=5, 10, 15, 20, 25, 30$ , respectively, using four different softening parameters.

### 3.3. Pitch Angles of the Patterns

In Figure 11 we plot the  $m=2$  potential phase-versus-radius at different time steps for the four runs, in order to study the variation of pitch angle of the spiral-bar pattern versus radius.

For most plots, it can be seen that the slopes of the  $m=2$  phase-versus-radius starting from  $r=10$  (which is close to the inner Lindblad resonance location of the dominant mode) to  $r=40$  (which is close to the outer Lindblad resonance, or the outer limit of the mode) are within a narrow range, especially if we exclude the step  $n=8000$  (solid) lines, which may be contaminated by the noisy features during the mode emergence phase. This near constancy of the slopes of the phase-versus- $r$  curves indicates the presence of logarithmic spirals, or else skewed-bars, with nearly constant pitch angle. Some of the regional bumps on the curves could be due to contamination from local instability clumps or noise.

Of particular interest is the plot for  $a_{soft} = 0.1$ , which, as we had previously shown, harbors a pronounced bar pattern in the later stage of the run. The evidence of the spiral-to-bar morphological change can be seen here from the phase-versus-radius plot. At the earlier stages of the run (step 8000 and earlier) there is a more steep gradient for the phase versus radius curves, indicating the presence of a (skewed) spiral pattern, whereas for the later stage of the run the phase versus radius curves flatten out, reflecting the reduced skewness of the bar. However, a comparison with the  $a_{soft} = 0.1$

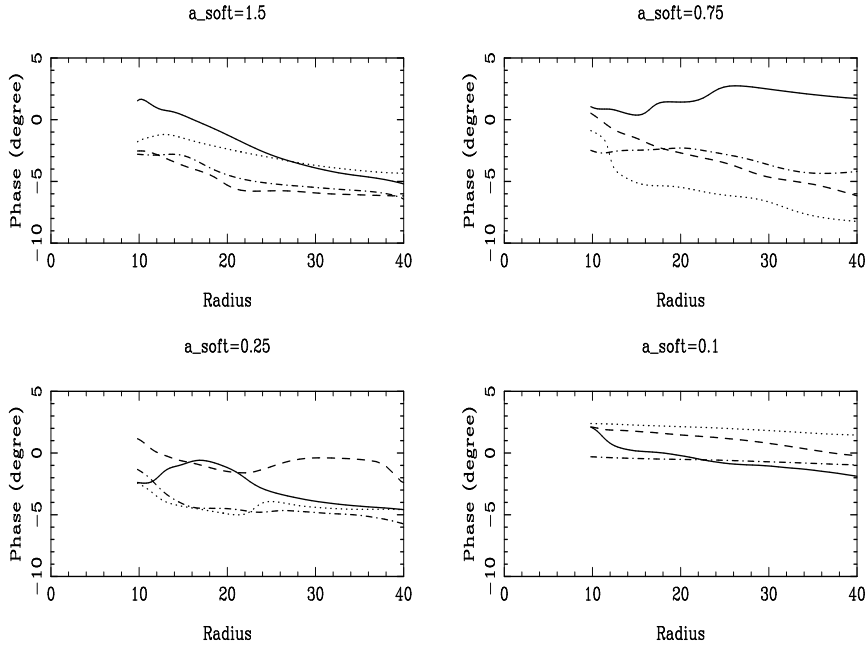


Figure 11: Phase versus radius of the  $m=2$  potential at time steps 8000 (solid), 16000 (dashed), 24000 (dotted), 32000 (dash-dotted), for runs with four different softening length choices.

phase-versus-time plot (Figure 10) shows that between  $r=10$  to  $r=30$  the phase-versus-time curves have nearly constant slope throughout the simulation run, indicating a constant pattern speed throughout both the spiral and bar phases for this evolving mode. This constant pattern speed during the modal morphological evolution is also supported by the time-segmented power spectrum analysis of Figure 13, which we will present next. These results thus corroborating one another to show that the spiral and bar modes are from the same modal family (i.e, the spiral evolves smoothly to a bar, rather than spiral disappearing and a bar of a different pattern speed later appearing). Therefore, even with the modal shape evolving from spiral to bar, we are still led to the quasi-steady modal picture, rather than a transient and recurrent pattern picture<sup>8</sup>.

---

<sup>8</sup>In essentially all the numerical simulations of spontaneously-formed density waves in disk galaxies, the unstable bar modes were obtained from initially going through a spiral phase (see, for example, Sparke & Sellwood 1987). This is because the formation of density wave modes requires the removal of angular momentum from across the inner disk (within corotation) and the deposit of angular momentum to the outer disk region outside corotation, and this removal and deposition of angular momentum in turn depends on the

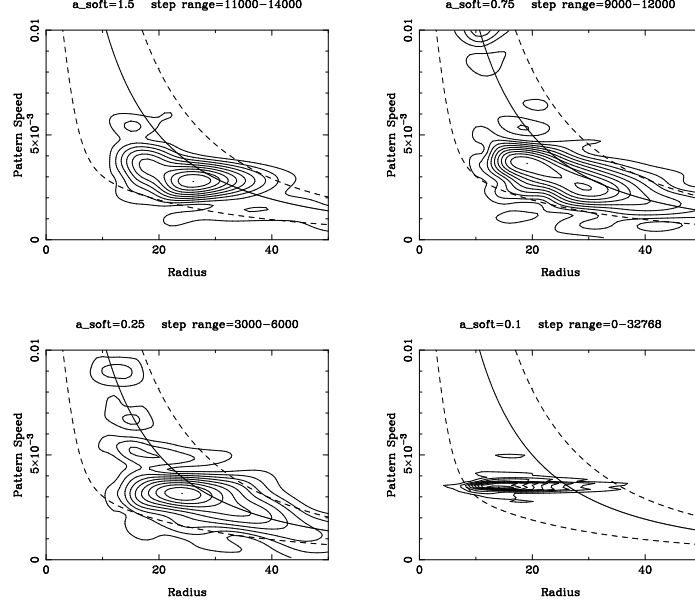


Figure 12: Contour plot showing comparison of the power spectra from  $m=2$  potentials at different radii during indicated time intervals, for the four different softening parameters and with 20 million particles. The solid line indicates galactic rotation speed  $\Omega$ , the two dashed lines are  $\Omega \pm \kappa/2$ , where  $\kappa$  is the epicycle frequency.

### 3.4. Power Spectra

In Figure 12 we present the contour plots of the power spectra of the  $m=2$  potential perturbations, from the above four runs with differing softening parameters during selected time intervals, and over the galactic radial range where the dominant mode is expected to have significant amplitude. The solid line in each figure indicates the galactic rotation curve in angular speed, the dashes curves delineate the range where modal amplification within the galactic resonant cavity is most likely to occur (Bertin et al. 1989a,b).

---

presence of potential-density phase shift of the pattern involved (Z98), and the phase shift value is smaller for bars than for spirals (since bars generally are less skewed than spirals). Therefore a bar mode employs a spiral modal shape during its youthful developmental stage to remove angular momentum needed for its growth, until it reaches the adequate amplitude and modal shape to become its mature self. This process incidentally lends support to many of the so-called “super-fast bars” found in the Zhang & Buta (2007) and Buta & Zhang (2009) samples, which have the bar corotation radius located intermediate in the bar rather than at the bar end as dictated by conventional wisdom from passive orbit analysis. If all bars are formed through an initial spiral phase, and if the corotation radius during spiral phase are located midway in the spiral arms, then we should not be surprised to find a fraction of bars to have this property as well, since the transition stage between spirals and bars can appear as either an open spiral or a skewed bar.

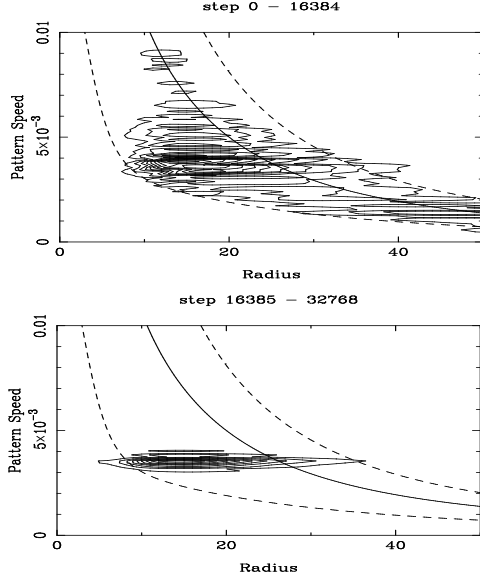


Figure 13: Power spectra from  $m=2$  potential at different radii for the 20 million particle and  $a_{soft} = 0.1$  run. Top: step = 0 - 16384, or the spiral-dominated phase. Bottom: step = 16385 - 32768, or the bar-dominated phase. The solid line indicates galactic rotation speed  $\Omega$ , the two dashed lines are  $\Omega \pm \kappa/2$ .

Note that for the larger softening runs ( $a_{soft} = 1.5, 0.75, 0.25$ ) we have only plotted during the time interval where the first dominant mode emerges and reaches quasi-steady state. This mode will further evolve and change pattern speed (in the general trend of increasing pattern speed as the disk mass becomes more centrally concentrated) during the remainder of the simulation run<sup>9</sup>. Later in the text (Figure 33 - 36) we will present further evidence of modal evolution with time. Note also that the pattern speed for the  $a_{soft} = 0.75$  case varies slightly with radius (i.e. the power spectrum has a nonzero slope), indicating the tendency for the winding up of the pattern with time for this softening run.

Cross-comparison with the phase-versus-time/phase-versus-radius plots of the previous two sub-sections shows that changes in pattern speed and spiral winding angle appear *continuously* both in time as well as in space throughout the simulation run, rather than appear as random fluctuations that a transient spiral pattern would produce.

For the small softening length  $a = 0.1$  run, despite the transition from spiral-shaped to bar-shaped morphology, the pattern speed of the mode is

---

<sup>9</sup>This is the reason we have only plotted the mode for limited time range so as to avoid pattern-speed smearing. The end of the above plotting range does NOT indicate the end of the modal activity.

seen to remain constant. This can be seen especially clearly if we break up the time duration of the power spectrum calculation into two segments, as shown in Figure 13. It can be seen here that the main power spectrum speak stayed at nearly the same vertical scale (indicating the same pattern speed) for both time segments. The conclusion of the constancy of the pattern speed throughout the spiral-to-bar morphological evolution during the  $a_{soft} = 0.1$  run is further confirmed when we re-examine the  $m=2$  phase-versus-time plot (Figure 10). This shows that with the choice of small particle softening (and in physical galaxies, the *zero* effective particle softening in the Newtonian force law), and with the thickness of the disk here partly represented by grid softening, allow self-organization and global-self-consistency of the galaxy density wave mode to be accomplished and maintained during both the spiral and bar evolution phases.

### 3.5. Potential-Density Phase Shift and Radial Mass Flow

Having established the modal characteristics for the simulated density wave patterns, we now look into the issue of radial mass flow in the parent disk galaxies containing these patterns.

In Figure 14, we present the contour plots of the morphologies of the  $m=2$  modal density and potential (with the potential negated so as to ease the comparison with density) for the four runs at a progressively decreasing time step for each case, corresponding to the initial emergence period of the mode for the particular softening-parameter choice. We can see that a spiral-like morphology is present in all cases (this morphology will later evolve into a more bar-like morphology for the  $a_{soft} = 0.1$  run). Furthermore, we see that the potential patterns display a more open appearance than their corresponding density patterns, which are more tightly-wound. *This difference in the winding of the density and potential patterns reveals the radial distribution of the azimuthal potential-density phase shift*, which we had plotted schematically in Figure 2, and which we will analyze quantitatively below. Formal definition of the equivalent azimuthal phase shift between the perturbation potential and density patterns in disk galaxies is given in Appendix A of the current paper (equation 3).

The existence of the quasi-steady azimuthal phase shift distribution, with potential lagging density within the corotation radius, and potential leading density outside corotation, means that there is a secular torque applied by the perturbation potential on the basic state mass distribution, thus a resulting secular angular momentum exchange between the wave and the basic

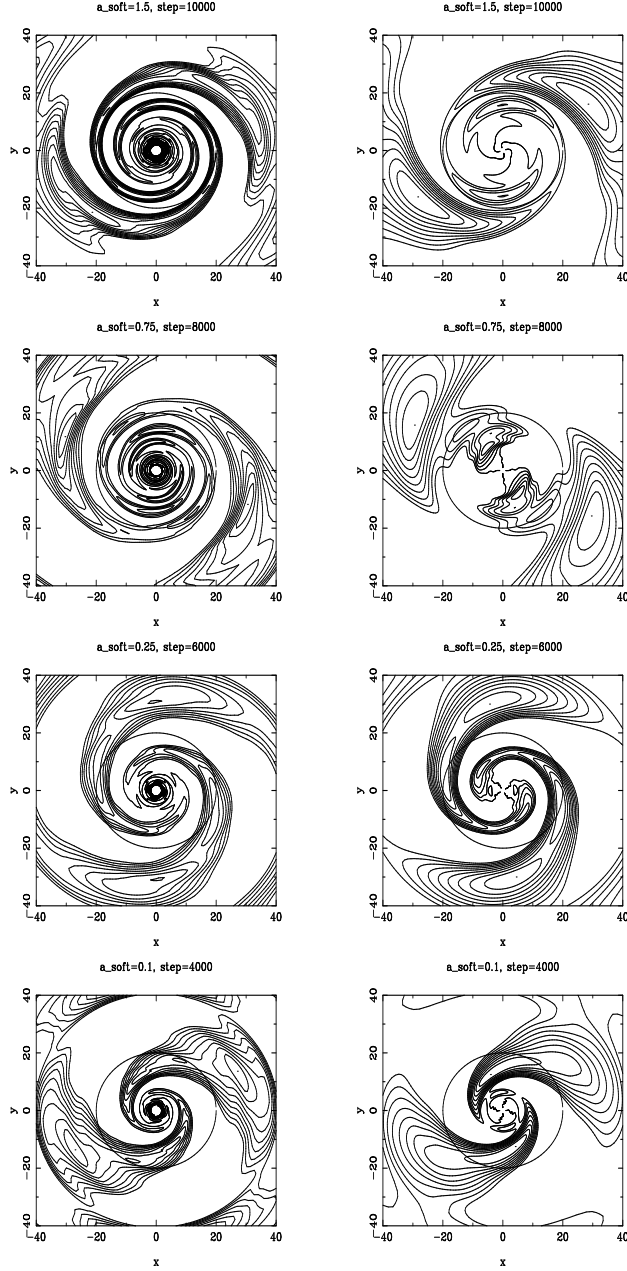


Figure 14: Morphology of the density (left frames) and (negative) potential (right frames) of the  $m=2$  modal component for the four runs at the respective time steps (10000, 8000, 6000, 4000) as indicated on the figure. Only positive contours are plotted. The circle in each case corresponds to the approximate location of the corotation resonance for that particular choice of the softening.

state at the quasi-steady state of the wave mode. This in turn leads to the inflow of basic state mass inside corotation, and the outflow of matter outside corotation.

In Figures 15, 16, 17, and 18, we plot the results of the radial dependence of the azimuthal potential-density phase shift, as well as the corresponding instantaneous mass flow rate, calculated using the perturbation density  $\Sigma_1$  and perturbation potential  $\mathcal{V}_1$  at each radius according to the expressions given in Appendix A (equations 3, 8), at a progressively decreasing time step for each of the four softening choices of 1.5, 0.75, 0.25, and 0.1, respectively. The time step for plotting is chosen near the peak of the first emerged density wave mode in the respective run.

Note that if the density-wave modal surface-density and kinematic distributions are truly globally self-consistent and quasi-stationary, and if the galaxy admits only one dominant mode, the phase shift (as well as mass flow rate) distribution will experience zero-crossing exactly at one corotation radius. The radial distribution of the phase shift would be a positive hump followed by a negative hump, with the transition between the two humps occurring at the unique corotation radius. In our simulations, we observe secondary oscillations in the phase shift curve in the central region of the disk as well as in the outer region. These have various causes: (1) Noise in the perturbation density and potential used, especially near the region where (and when) the perturbation quantities themselves are small; (2) Outer disk truncation effect in a finite-domain simulation (Z98); (3) Non-steady nature of the modes formed; (4) the formation of nested patterns inside the primary pattern.

From the derivation expressions given in Appendix A, we see that the mass flow pattern *has exactly the same zero crossings* as the phase shift pattern, yet different radial amplitude profile, due to the fact that for the mass flow rate expression the local surface density, the fractional density-wave amplitude, and the galactic rotation curve also play a role, in addition to the phase-shift or normalized torque-integral contribution. Thus the appearance of large-value, multiply-oscillating phase shift features near the galactic central (or outer) region does not necessarily signal their importance if the wave amplitude there is small, and the phase shift oscillations are mainly due to noise. This point is made self-evident from comparison of the left and right frames in Figures 15 - 18.

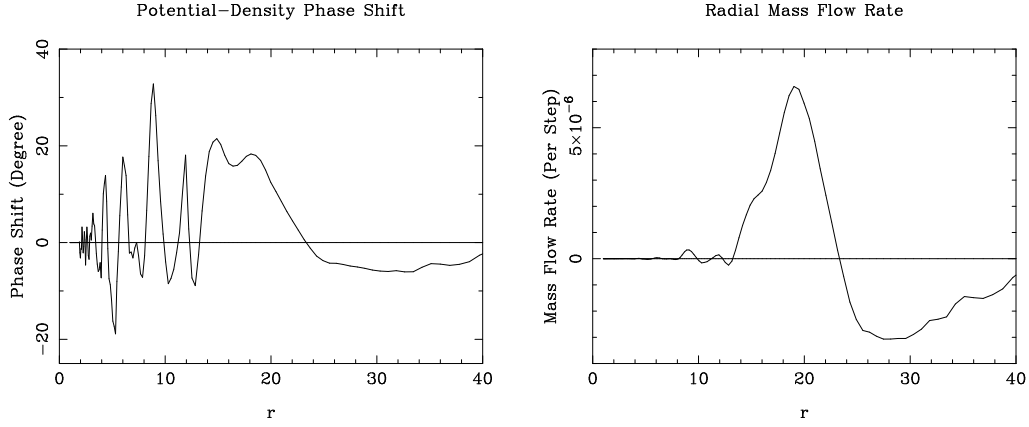


Figure 15: Potential-density phase shift (left frame) and mass flow rate (right frame) versus  $r$  at time step 12800 for  $a_{soft} = 1.5$  run. These two figures have identical zero crossings though different amplitude distributions.

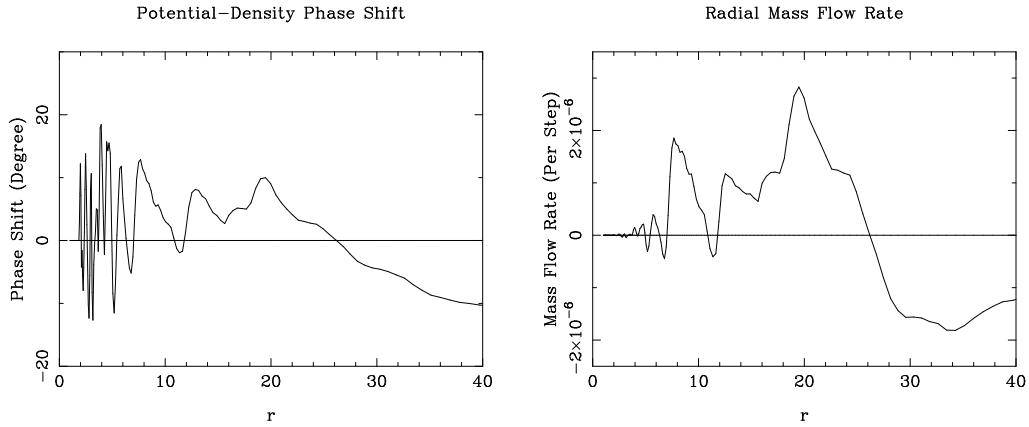


Figure 16: Potential-density phase shift (left frame) and mass flow rate (right frame) versus  $r$  at time step 10400 for  $a_{soft} = 0.75$  run. These two figures have identical zero crossings though different amplitude distributions.

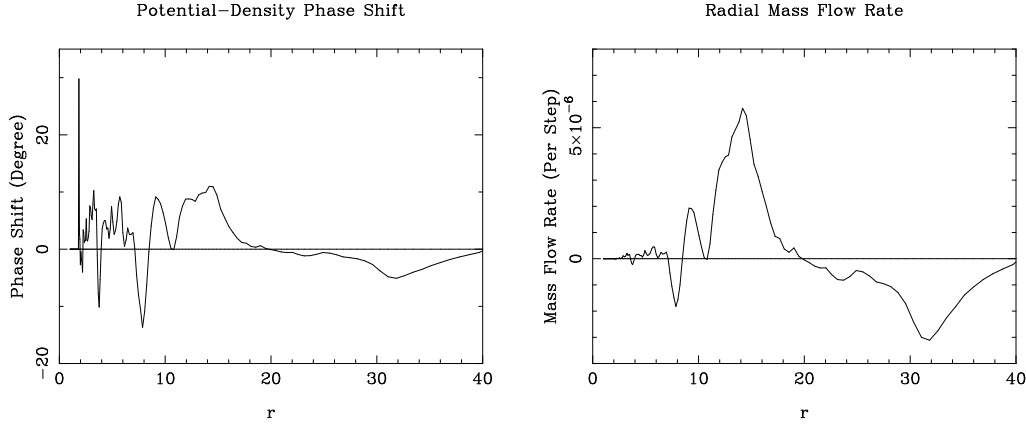


Figure 17: Potential-density phase shift (left frame) and mass flow rate (right frame) versus  $r$  at time step 5600 for  $a_{soft} = 0.25$  run. These two figures have identical zero crossings though different amplitude distributions.

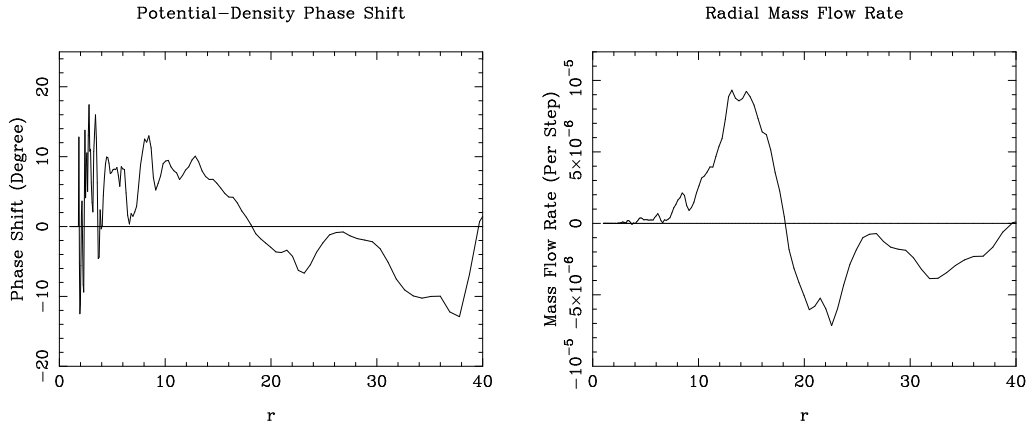


Figure 18: Potential-density phase shift (left frame) and mass flow rate (right frame) versus  $r$  at time step 8000 for  $a_{soft} = 0.1$  run. These two figures have identical zero crossings though different amplitude distributions.

### 3.6. Comparison of Analytical and Numerical Accretion Rates

The evidence we have presented so far supports the view that the spiral and bar patterns obtained in these N-body simulations were intrinsic modes of the basic state of the disk, and they emerge spontaneously out of originally featureless (axisymmetric) disks beyond the threshold for non-axisymmetric instabilities. These instabilities display long-range correlation and are self-organized. That natural laws implicitly allow such organization to spontaneously appear is part of the reason the universe displays the observed complexity and hierarchical organization, starting from the very simple set of fundamental laws and nearly homogeneous initial conditions of the Big Bang.

In what follows, we present an another set of analyses of N-body results, specifically to check whether the radial mass flow rates obtained in these simulations (responsible for bulge building as well as for the spreading out of the outer disk) agree with the analytical prediction (equation 8 in Appendix A), using the parameters of the global density wave modes in the same simulations. An agreement between the two lends support both to the analytical formalism, as well as to the relevance of using N-body simulations to characterize the self-organized density wave modes.

In Figure 19 we plot the time evolution of enclosed mass at two different radii (one inside and one outside corotation), after subtracting their respective values at the beginning of the simulation for each time step represented, for the previous simulation run using softening length  $a_{soft} = 1.5$ . We observe a general trend of mass inflow inside corotation resonance (CR) radius, and mass outflow outside CR. Note that the CR radius for this large softening choice is between 25-30, with larger value towards the earlier part of the simulation run. We therefore choose to plot the outside-CR mass flow curve at radius 32.5. For progressive smaller softening choices, the CR radius reduces accordingly. So for later plots ( $a_{soft} = 0.75, 0.25, 0.1$ ) we will choose to plot the outside-CR mass flow curves at radius 27.5.

In Figure 20, we plot the *expected* mass increase within the above two radii by *integrating in time* of the instantaneous mass inflow rate predicted by equation (8), using the density-wave modal characteristics (i.e., the perturbation potential and density distributions) as well as galaxy parameters obtained in the same simulation run.

Note that the time resolution for data points in Figures 19 and 20, as well as for subsequent similar pairs of figures, are slightly different. Figure 20 and similar figures below are obtained from instantaneous mass flow rates

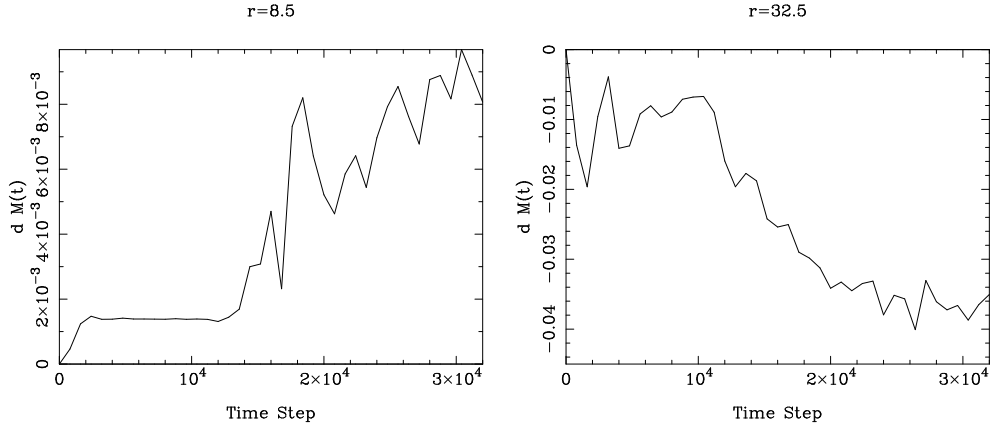


Figure 19: Time evolution of the enclosed mass for a typical radius inside corotation, and a typical radius outside corotation, relative to the initial time step  $n=0$  mass at the same respective radius, for the softening length  $a_{soft} = 1.5$  run

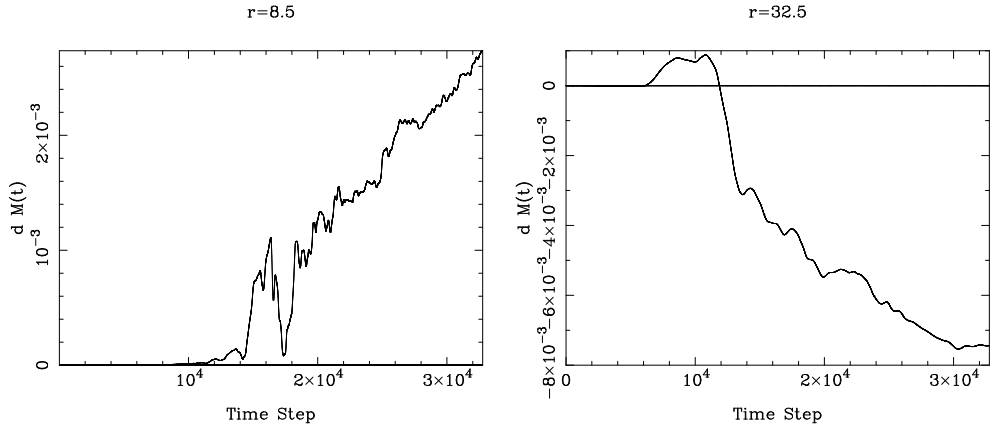


Figure 20: Predicted integrated mass evolution according to equation (8) within the two different radii, for softening length  $a_{soft} = 1.5$  run

calculated at every step of the simulation, and these are only recorded at selected radii. Figure 19 and similar figures, on the other hand, are obtained using the whole disk surface mass maps written out at selected time intervals ( $\Delta t = 800$  time steps in this case), so the time resolution is coarser. Nonetheless the gross features of these two kinds of plots can be compared without losing crucial information.

We observe from the comparison of Figure 19 and Figure 20 that at the location inside CR,  $r=8.5$ , the observed mass increase rate is about 3 times as large as the analytically predicted rate, though the trends of the mass increase are similar between the two. This large quantitative discrepancy is particular to the  $a_{soft} = 1.5$  run, likely related to the prohibition of the growth of the dominant  $m=2$  intrinsic instability by the large softening. With the suppression of the growth rate of the dominant  $m=2$  mode, some 3-armed as well as other noisy patterns are seen to emerge. These non-modal patterns can produce radial mass flow yet may not enter into the analytical mass flow prediction.

The mass flow behavior outside corotation likewise shows disagreement between the two plots: The actually measured mass increase in Figure 19 shows a consistent outflow pattern as befitting its location outside corotation, whereas the expected mass flow calculated using the torque equation showed initially a mass inflow, and only afterward changed to outflow. This shows that the nonlinear modal organization does not exactly reproduce the quiescent linear modal picture of the smooth launching of the mass flow activity. Also, once again the magnitude of the actually measured outflow rate is significantly higher than predicted for this case.

We had performed another simulation run with  $a_{soft} = 1.5$ , but with *the potential calculation keeping only the even azimuthal harmonics* during the Fourier transform process to obtain the grid potential, to reflect the fact that observed spiral and bar patterns show predominant bi-symmetric patterns. The results for the observed and predicted mass accumulations inside and outside CR are shown in Figures 21 and 22. Here the predicted and measured mass flow rates within CR are seen to be in better agreement, apparently due to the fact that the enforcement of even-harmonics-only coerced a much more effective growth of the collective instability which has bi-symmetry. It is now clear that as long as the global instability has accomplished its growth potential implicit in the mode/basic-state correspondence, through either the tinkering of symmetry (as shown here) or through the reduction of softening (as shown below), the agreement between the theoretical prediction and the

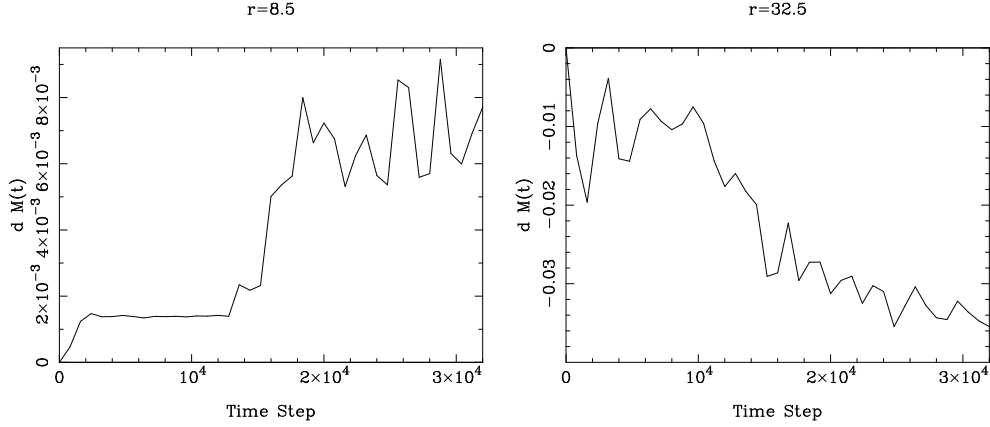


Figure 21: Time evolution of the enclosed mass for a typical location inside corotation, and a typical location outside corotation, relative to the initial  $n=0$  mass at the same respective radius, for the softening length  $a_{soft} = 1.5$  run, using only the even harmonics in potential calculation throughout the N-body simulation

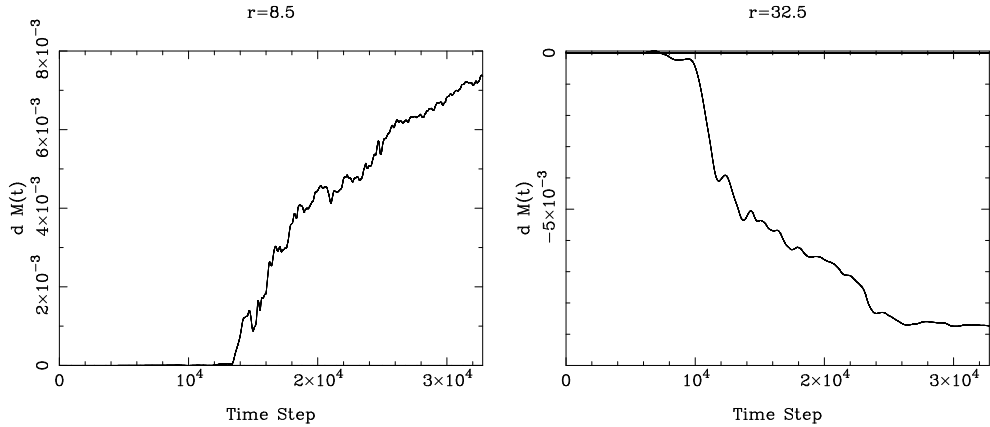


Figure 22: Predicted integrated mass evolution according to equation (8) within the two different radii, for softening length  $a_{soft} = 1.5$  run, using only the even harmonics in potential calculation throughout the N-body simulation

actual measurement in N-body simulations will tend to be good.

The even harmonics enforcement is most effective in encouraging larger wave amplitude for the  $a_{soft} = 1.5$  choice. For the other smaller softening choices we will present next ( $a_{soft} = 0.75 - 0.1$ ), the even harmonics enforcement in fact hampers the wave amplitude growth in the *later stages* of the calculation because there is the natural tendency in the small  $a_{soft}$  runs to form local instability clumps in the outer disk, and through the enforcement of bi-symmetry these would-be local clumps were seen to morph into diffused noise which tend to heat the outer disk and inhibit larger wave amplitude to be maintained. Still, tests show that even for  $a_{soft} = 0.75$  the enforcement of even harmonics encouraged a more vigorous modal growth during the first 1/3 of the simulation run, and as a result the mass flow rate for that duration of time has better agreement between the predicted and measured values.

In Figure 23 we plot the actually measured enclosed mass evolution compared to its value at the beginning of the simulation, for  $a_{soft} = 0.75$  run, with the left frame shows the typical mass flow trend inside CR, and the right frame is typical of the behavior outside CR. In Figure 24, we plot the expected accumulation of mass within the two radii by integrating the instantaneous mass inflow rate according to equation 8.

We see that at  $r=8.5$ , the trend of mass accumulation with time between these two figures are extremely similar. Furthermore, the value of analytically inferred rates is only about 30-40% smaller than the actual observed rates. This is a much better agreement than the case we had shown before for the  $a_{soft} = 1.5$  run using all harmonics. This shows that decreasing softening does make a significant difference in our ability to correctly model the collective effects. As we have commented before, enforcing by-symmetry in the potential calculation will lead to further improved agreement between the predicted and measured mass flow rates, for the initial 1/3 of the simulation duration, before the heating effect sets in.

In the  $a_{soft} = 0.75$  run, the predicted mass accretion for  $r=27.5$  has some large fluctuations due to the contamination of multi-armed patterns. We therefore chose to use only *even harmonics in the accretion calculation for the  $r=27.5$  location (even though the N-body simulation itself was run with the full harmonics set)*. This procedure in the analysis helps to filter out effect of the transient features and leads to better agreement between the measured and predicted mass accumulation rate at  $r=27.5$ , though some residual fluctuations still exist. Once again the magnitude of the outflow is smaller for the predicted than the measured for this run, as for  $a_{soft} = 1.5$ .

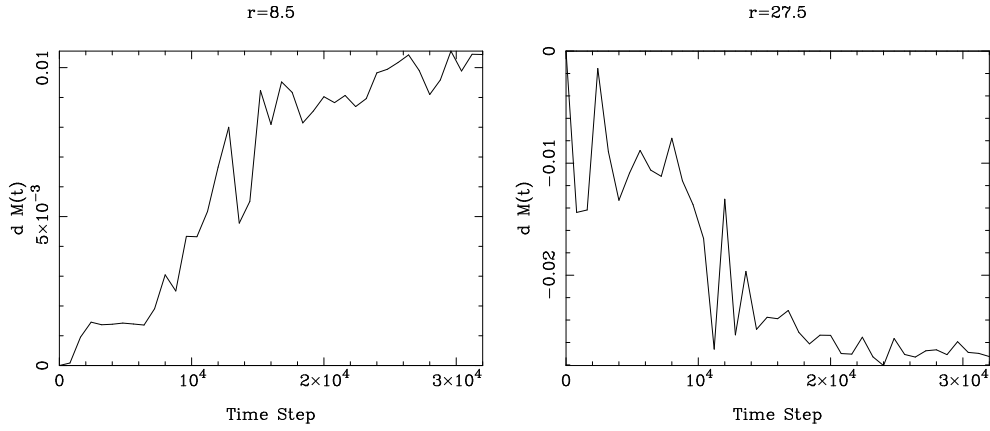


Figure 23: Time evolution of the enclosed mass for a typical location inside corotation, and a typical location outside corotation, relative to the initial  $n=0$  mass at the same respective radius, for the softening length  $a_{soft} = 0.75$  run.

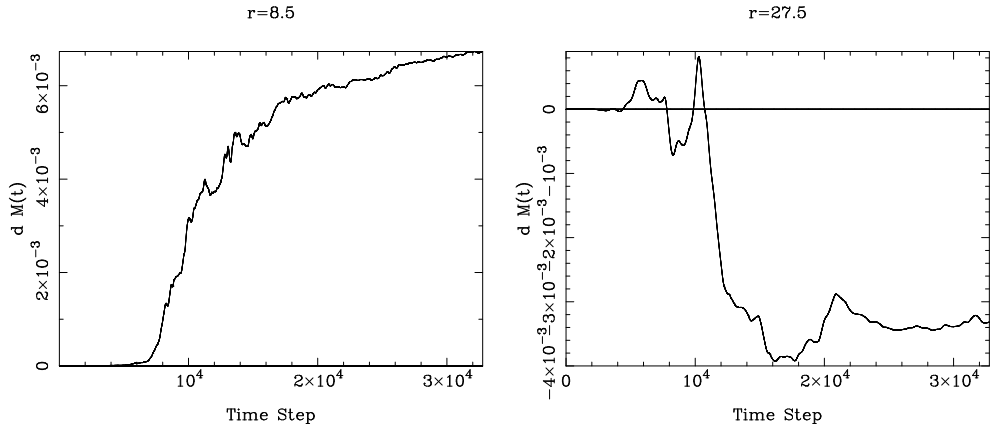


Figure 24: Predicted integrated mass evolution according to equation (8) within the two different radii, for softening length  $a_{soft} = 0.75$  run. The second frame (for  $r=27.5$ ) used only even harmonics in the mass flow calculation.

In Figure 25 we plot the actually measured enclosed mass evolution at the two different radii compared to its value at the beginning of the simulation, for the  $a_{soft} = 0.25$  run. In Figure 26, we plot the predicted accumulation of mass within the two radii by integrating the theoretical instantaneous mass inflow rate equation 8.

For this run, for the location  $r=8.5$  the measured enclosed mass evolution curve has similar profile as that predicted. Furthermore, we see that the numerical values of analytically inferred and actually-measured mass accumulation rates are *nearly identical*. This shows that reducing the softening length to  $a_{soft} = 0.25$  allows the inter-particle interactions to fully represent the collective effect implicit in the global modal characteristics.

The predicted mass accumulation curve outside CR ( $r=27.5$ ) was more noisy than the inner region behavior due to the formation of several local instability clumps at the outer region of the computation domain. So we have once again *used only the even harmonics for the mass accretion calculation for the  $r=27.5$  location* (not for the N-body simulation itself, which was performed using full harmonics), which filtered out the contamination of the local transients. Here we witness that the numerical value for the predicted and measured outflow rates are in better agreement than for the previous two larger-softening cases.

In Figure 27 we plot the actually measured enclosed-mass evolution at the two different radii, compared to their values at the beginning of the simulation, for the softening choice of  $a_{soft} = 0.1$ , as the most extreme case of softening parameter tests.

Note that the inflection of the curves near time step 5000 for the  $a_{soft} = 0.1$  run, inside CR, is linked to the launch of spiral to bar modal shape transition. The spiral phase is seen to lead to higher rate of mass inflow compared to the bar phase, due to the more significant skewness and thus the resulting larger potential-density phase shift of the spiral pattern as compared to the bar pattern. This higher mass flow rate for the spirals as compared to bars was also confirmed in the physical galaxy samples analyzed in Zhang & Buta (2007, 2015).

The mass flow curves outside CR for  $a_{soft} = 0.1$  have similar trends, though the predicted rate once again is smaller in magnitude.

In Figure 28, we plot the expected mass accumulation of mass within the two different radii for the  $a_{soft} = 0.1$  run by integrating the instantaneous mass inflow rate equation 8. We see that the observed and predicted mass flow curves within the  $r=8.5$  region are quite comparable, with the predicted

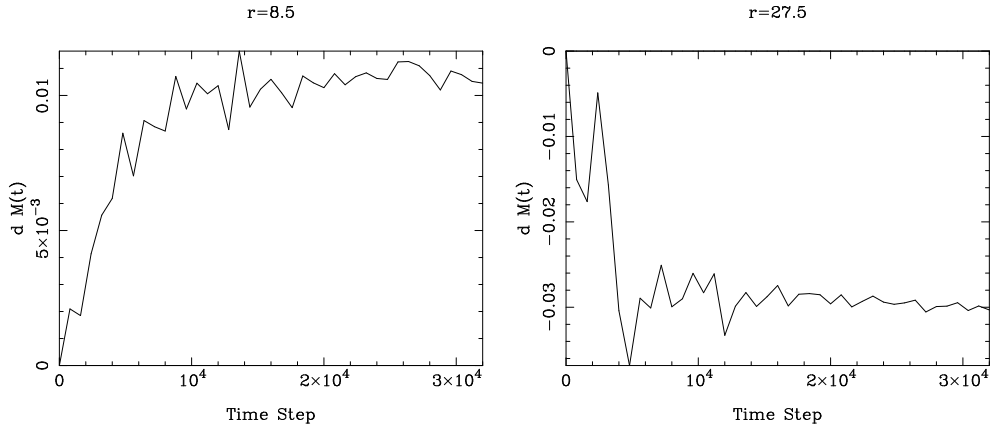


Figure 25: Time evolution of the enclosed mass for a typical location inside corotation, and a typical location outside corotation, relative to the initial  $n=0$  mass at the same respective radius, for the softening length  $a_{soft} = 0.25$  run

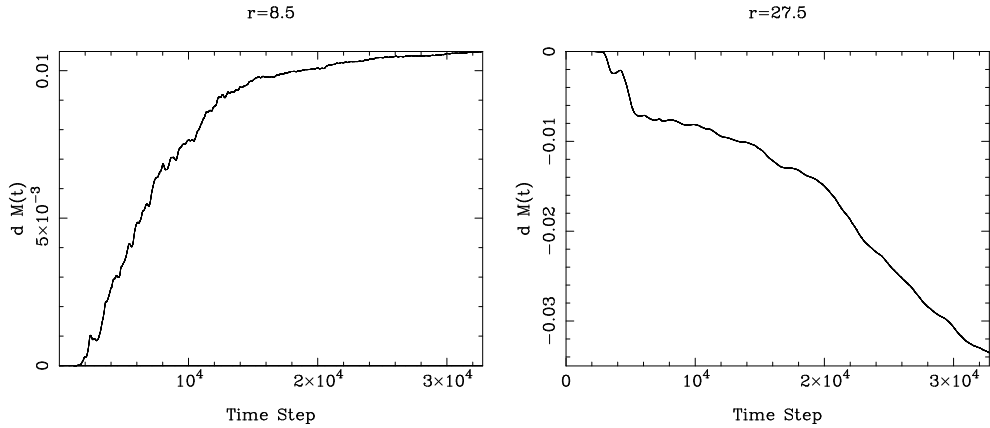


Figure 26: Predicted integrated mass evolution according to equation (8) within two different radii, for softening length  $a_{soft} = 0.25$  run. The second frame (for  $r=27.5$ ) used only even harmonics for mass flow calculation.

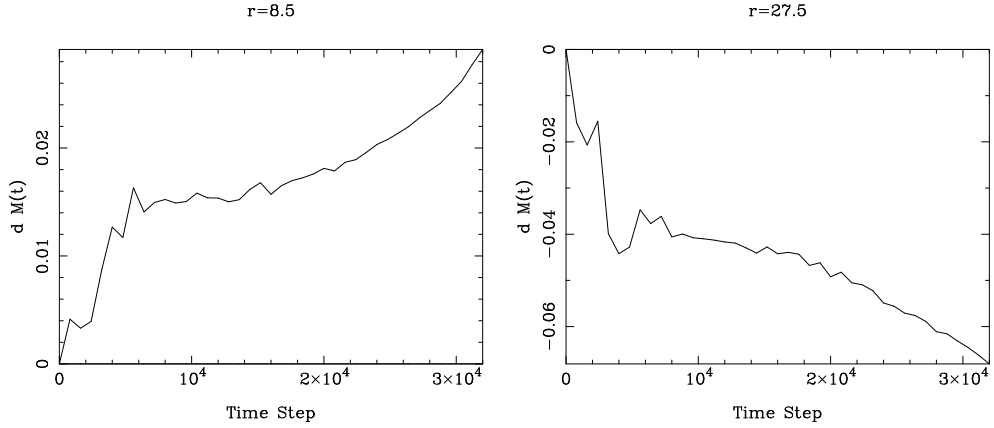


Figure 27: Time evolution of the enclosed mass for a typical location inside corotation, and a typical location outside corotation, relative to the initial  $n=0$  mass at the same respective radius, for the softening length  $a_{soft} = 0.1$  run

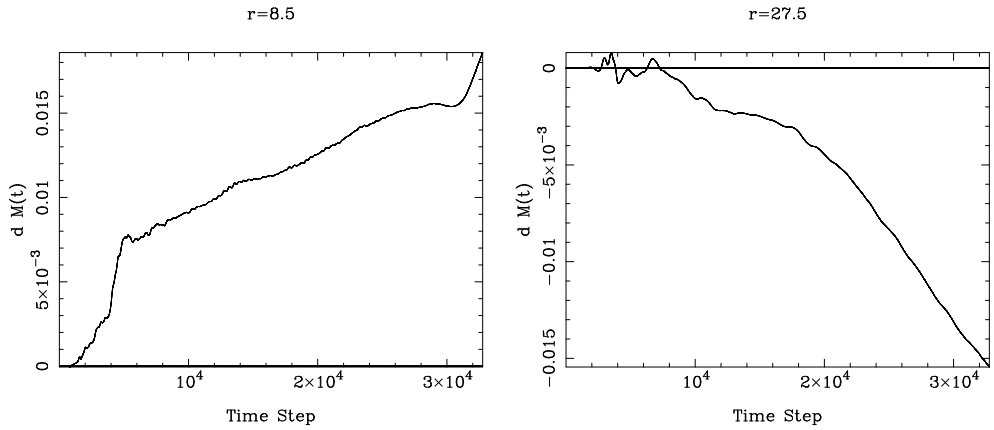


Figure 28: Predicted integrated mass evolution according to equation (8) within the two different radii, for softening length  $a_{soft} = 0.1$  run

rates smaller than the actual rates by about 30%. Here the difference is obviously not due to the suppression of collective effects, because the softening length used is even smaller than in the  $a_{soft} = 0.25$  case. The likely cause for this residual discrepancy may be attributed to the viscosity-induced accretion effect (or dynamical friction) not accounted for by the density-wave torque calculation.

Reexamine all of the outside-CR curves for the previous runs, we see that they share the same feature of a more pronounced drop in (measured) enclosed mass at the beginning of the run, signaling a rapid mass outflow episode as the self-organization of the mode begins to take place, that was not reflected in the corresponding predicted mass outflow (this large drop in measured enclosed mass was seen to be the main reason of the difference in magnitudes of the measured and predicted outflows in each case, because after this initial drop the slopes of the outflows are seen to be quite comparable between the measured and predicted). This common discrepancy may be partly a result of the fact that the outer disk has very low surface density, and the density wave is poorly represented there, so the self-organization process may depart more significantly from the smooth modal-emergence picture.

We also note from the above runs that the net amount of mass *increase* within  $r=8.5$  does not have as substantial a difference between the different softening runs (apart from the extreme case of  $a_{soft} = 0.1$ ), compared to that given in Figure 3 and Figure 4 for  $r=3.5$ . This difference is partly accounted for by the shape of the modified exponential surface density for the choice of basic state, and as the secular evolution proceeds the entire curve squeezed inwardly, as opposed to a surface density increase at every radius as a result of mass inflow (see below the surface density evolution in Figure 30).

We choose this larger radius  $r=8.5$  to confirm the analytical mass flow equation because near the very central region the presence of nested resonances complicate the analysis. Even  $r=8.5$  itself is officially within the inner Lindblad resonance of the outer mode<sup>10</sup>. A location further out in radius turned out to exhibit even earlier saturation of the accretion behavior because the disk surface density is depleted as a result of the accretion pro-

---

<sup>10</sup>The resonance itself is shielded from being active to the wave by the rapid increase in velocity dispersion in this region, which forms the so-called “Q-barrier” that allows the inwardly propagating (short trailing) density wave train to be reflected to become outward propagating (long trailing) wave train towards corotation region to complete the feedback loop and to form growing modes (Mark 1976).

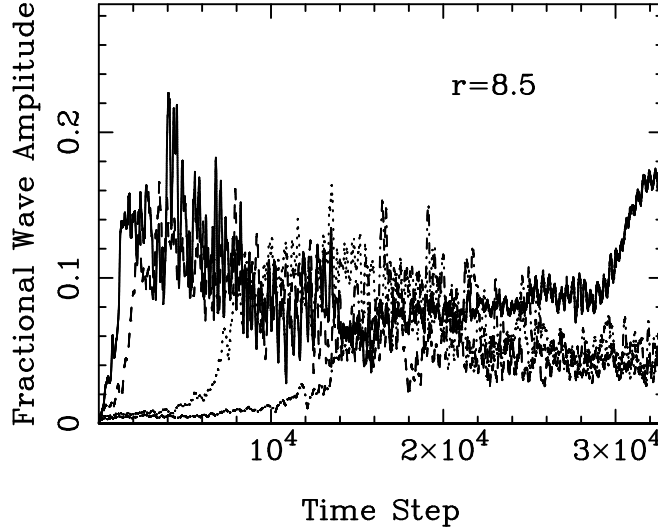


Figure 29: Evolution of the fractional wave amplitude for the four softening choices, at radius  $r=8.5$ . Solid:  $a_{soft} = 0.1$ , Dashed:  $a_{soft} = 0.25$ , Dotted:  $a_{soft} = 0.75$ , Dash-Dotted:  $a_{soft} = 1.5$ ,

cess (see Figure 30 below), thus becomes unable to support the full amount of mass inflow required by the density wave mode.

That  $r=8.5$  location can still be a good representative of the accretion flow due to the outer mode is seen also in the  $m=2$  morphology plot we presented earlier (Figure 14). There we see that the dominant mode does penetrate to within the central  $r=8$  region (the nuclear nested mode is well within the central  $r=5$  region), so the mass inflow predictions calculated for  $r=8.5$  are still those for the outer dominant mode. This dilemma of the simulation can be avoided in physical galaxies through the vertical accretion of cold gas onto the galaxy disk, followed by its inward channeling to replenish the depleted surface density of the disk, and to support continued mass accretion throughout the lifetime of a galaxy.

In Figure 29, we plot the evolution of the fractional wave amplitude (defined as the *geometric mean* of the density- and potential-wave fractional amplitudes) during the simulation run, for the four softening choices and at the radius  $r=8.5$ . Note the progressive delayed emergence of the wave mode, as well as the decrease of equilibrium amplitude, as the softening parameter is increased. Note also that for  $a_{soft} = 0.1$  case, the amplitude is re-invigorated towards the end of the simulation run, due to the strengthening of the central bar as a result of previous mass inflow – this fact can also be discerned from Figures 27 and 28 as the steepening of the enclosed

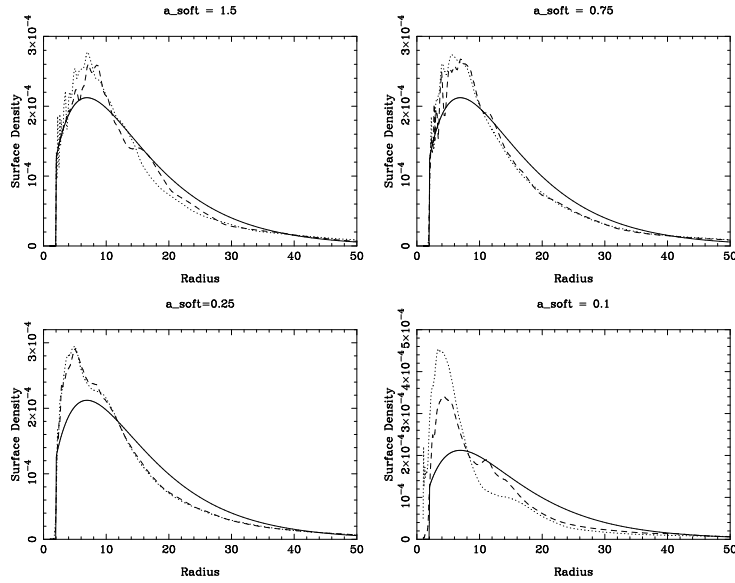


Figure 30: Comparison of the surface density evolution of the N-body runs using four different softening parameters, and all with 20 million particles. The different curves in each figure are for time steps of 0 (solid), 16384 (dashed), and 32768 (dotted), respectively. Note that the last frame (for  $a_{soft} = 0.1$ ) has a different vertical scale than the other three frames.

mass slope in the last quarter of the run, as compared to the corresponding figures for  $a_{soft} = 0.75$  [Figures 23, 24], and for  $a_{soft} = 0.25$  [Figures 25, 26], where the enclosed mass flattens out towards the end of the simulation, indicating the slowing down of accretion behavior (which is matched by their respective decreased wave amplitudes as shown in Figure 29). Of course, the mass flow rate is determined not only by the fractional wave amplitude, but also by the potential-density phase shift, as well as by other wave and basic state parameters (Appendix A, equation 9), all of them working in concert to produce the final radial mass flow rate.

In Figure 30, we plot the surface density evolution of the above four runs. This plot corroborates what we had found before from the plots of mass inflow within the central  $r=3.5$  and  $r=8.5$  radius, as well as outside the corotation radius. The  $a_{soft} = 0.1$  choice is seen to be the most effective in producing enhanced mass flow rates, due to its larger wave amplitude and most persistent density wave activity.

## 4. ANALYSES AND DISCUSSION

### 4.1. On the Modal and Quasi-Steady State Hypotheses of Density Waves in Physical and Simulated Disk Galaxies

#### 4.1.1. Previous Work

The mass flow rate equation used in the last section is exact when the density wave pattern involved is a *spontaneously formed mode* that has achieved *quasi-steady state* (Z98). When this state is achieved, the rate of global wave amplification through over-reflection at corotation is balanced by the local dissipation at the spiral-arm collisionless shock. The wave amplitude as well as its shape are unchanged (at least on the timescale of local dynamical time, or galaxy rotation period), and the only measurable secular change is the slow redistribution of disk matter both inside and outside corotation, as well as the heating of disk stars and the energy injection into interstellar medium (ISM). The quasi-stationary spiral structure (QSSS) hypothesis had been used in the past few decades by many workers to explain the grand-design spiral structures in galaxies (Bertin et al. 1989a,b and the references therein), though in these previous analyses the mechanisms for wave damping and for secular evolution of the basic state were not properly identified.

How good are the modal and QSSS hypotheses? Are there any objective ways we can judge these? Earlier workers (for example, Elmegreen & Elmegreen [1983,1989]) employed statistical arguments to support the QSSS hypothesis, and N-body simulations provided support to the modal and QSSS hypotheses to varying degrees (Donner & Thomasson 1994; Z98). Zhang & Buta (2007, 2015), Buta & Zhang (2009) used near- and mid-infrared images of galaxies to show that for nearby grand-design galaxies, the level of quasi-steady state for the density wave patterns involved can be judged from the coherence of the potential-density phase shift curves, and from the *level of agreement* between the phase-shift positive-to-negative zero-crossing predictions for the corotation resonance (CR) radii and the actual resonance features in galaxies. Independent studies have confirmed the accuracy of the potential-density phase shift method for determining the CRs in grand design galaxies (i.e., Haan et al. [2009], who compared several methods for CR determination previously published in the literature, and stated “For our galaxies the phase-shift method appears to be the most precise method with uncertainties of (5-10)% ...”; as well as Martinez-Garcia et al. [2009,1011] who used a color gradient method to determine CR, and among their sample galaxies which overlapped with that of Zhang & Buta [2007] or Buta &

Zhang [2009], there is good agreement in the CR locations determined by these two independent approaches).

#### 4.1.2. *Analogy with Fully-Developed Turbulence*

In what follows, we demonstrate another effective approach for determining the quasi-steady state (QSS) of the modes<sup>11</sup>, in addition to our previous approach of comparing the phase shift zero crossings with the resonant features on the galaxy images. This time, instead of using just the radial distribution of the potential-density phase shift, we will actually make use of the mass-flow-rate curve, even though the two curves have the same zero crossings, because as it turns out the magnitude of the mass flow rate curve provides crucial information about the quasi-steady modal status as well.

In Figure 31, we present the comparison of radial mass flow rates of six galaxies calculated using the torque equation (8), first using only the  $m=2$  Fourier components (dashed curves) for the perturbation density and potential, and subsequently using the full set of Fourier components (solid curves). The solid curves had previously been published in Zhang & Buta (2015). We see immediately that apart from minor differences, the agreement between the  $m=2$  calculation and  $m=\text{full}$  (short-hand for using all Fourier components) calculation agree to a high degree. In particular, slightly larger disagreements were obtained for the two galaxies (NGC 5194, or M51; and NGC 3627, which is part of the Leo Triplet interacting galaxy group) that are known to be undergoing tidal interactions. We also notice that along the trend of Hubble type evolution from late to early (left to right, top to bottom for these six galaxies in Figure 31), the agreement between the  $m=2$  and  $m=\text{full}$  mass flow rates gets progressively better.

In Figure 32, we present similar comparison of  $m=2$  and  $m=\text{full}$  mass flow rates for galaxy NGC 1530, first analyzed in Zhang & Buta (2007). This galaxy has exceptionally high mass flow rate even though it is in a relatively isolated environment. We observe that the  $m=\text{full}$  mass flow rate was

---

<sup>11</sup>We use QSS in the following instead of the original QSSS abbreviation here because we are considering the quasi-steady state of both the spiral and bar modes. Note that in order for the phase shift and torque relation to be applicable, the quasi-steady state for the wave mode only need to be maintained on the order of local dynamical time scale (i.e. galaxy rotation period), so the secular changes in the modal shape due to the secular changes of the basic state does not hamper the applicability of the phase-shift/volume-torque calculation approach.

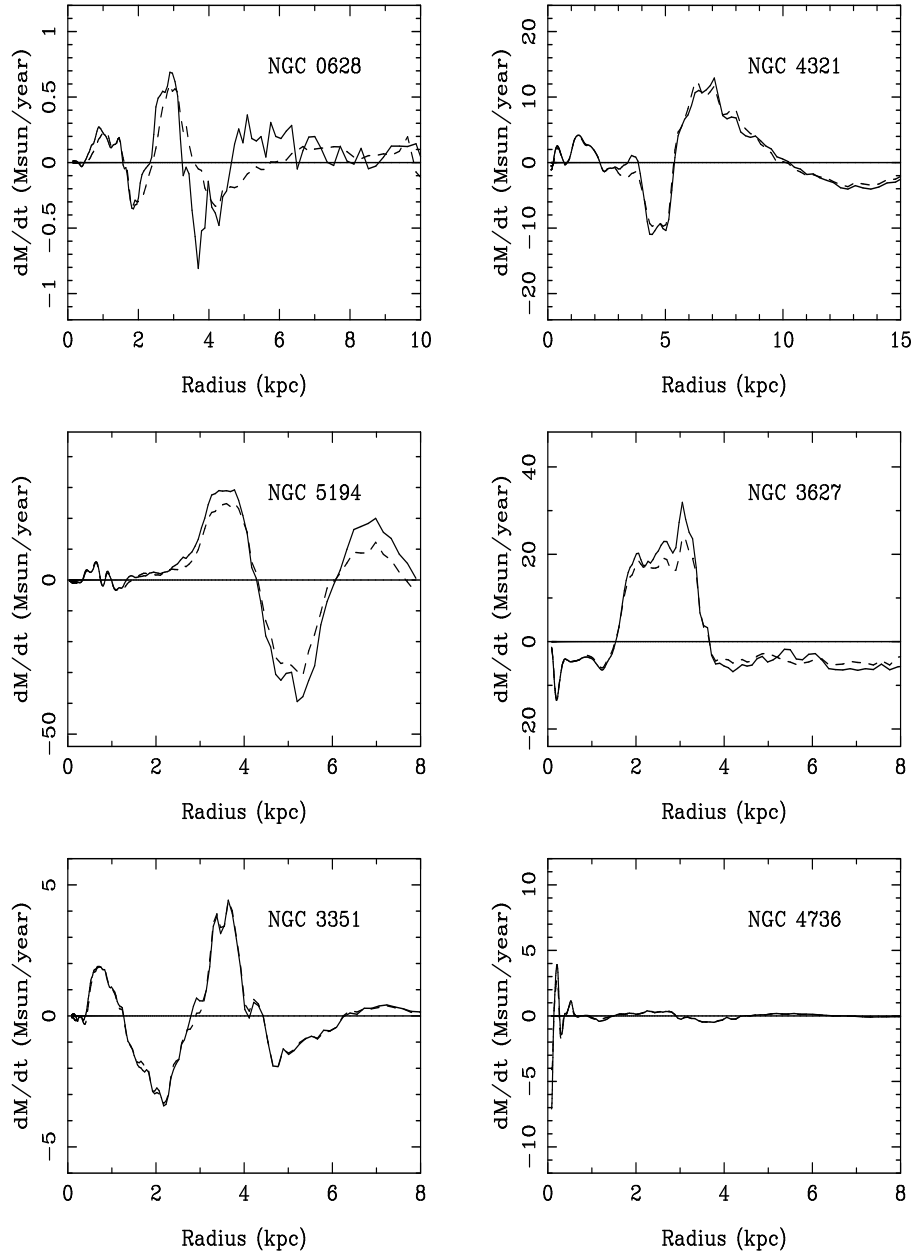


Figure 31: Radial mass flow rates for the six sample galaxies of Zhang & Buta (2015). The solid lines are calculated using the full Fourier spectra of density and potential, and the dashed lines using only the  $m=2$  components.

significantly higher than the  $m=2$  mass flow rate (though the zero-crossings of the two curves are similar), indicating that the amplitude of the mode is yet to settle into its quasi-steady value even though the modal density profile appears to be stabilized: The amplitude of the mode is obviously on the wane.

In Z98, we have demonstrated that the growth rate of the mode  $\gamma_g$  due to global amplification and feedback cycle is positively correlated with the *fraction* of  $m=2$  sinusoidal modal component in the density wave composition (since only the  $m=2$  modal component has the correct phase relation between the over-reflected wave train from corotation and the incoming wave train, in order to form growing mode; whereas the higher harmonic components cancel out due to their lack of correct phase relations). On the other hand, the effective dissipation rate  $\gamma_d$  of the mode, once the wave has acquired sufficient nonlinear amplitude, is approximately independent of the exact nonlinear distortions of the wave profile (since  $\gamma_d$  is determined mainly by the potential density phase shift pattern for a wave with a given amplitude, and the phase shift was shown to be relatively independent of the degree of nonlinearity in the azimuthal density profile of the mode [Figure 5 and Figure 6 of Z98]). Therefore, for high-amplitude, very nonlinear density wave mode such as present in NGC 1530, the mode is able to manipulate the degree of nonlinearity of its azimuthal profile to boost up the damping rate as compared to the growth rate, in order to evolve towards a quasi-steady equilibrium amplitude.

The results shown above, that at quasi-steady state of the wave mode the  $m=2$  and  $m=\text{full}$  contribution to radial mass flow are approximately equal, might appear at first sight to be surprising, i.e. how could something that is supposed to be only “a part” of the whole be equal to the whole? Here we need to realize the specialness of a self-organized density wave mode that has achieved quasi-steady state. The mode had gone through many cycles of fine adjustments among its various physical processes so that global the self-consistency condition is achieved. Among these processes, one of them is the randomization of the orbital energy of the basic state matter during the energy and angular momentum exchange between the wave mode and the basic state, through the mediation of the collisionless shock at spiral arms. This randomization process happens both for the stellar and for the ISM components of the galaxy disk mass, and there are in fact two aspect to it (Z99): one aspect is the randomization of the orbital energy corresponding to  $\Omega_p \times L_{\text{wave}}$ , where  $\Omega_p$  is the pattern speed of the wave and  $L_{\text{wave}}$  is the

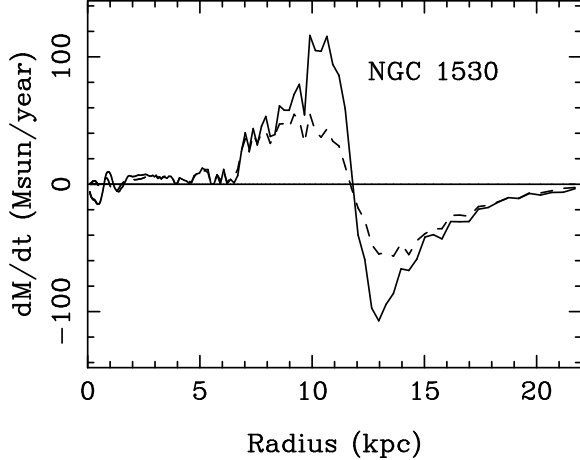


Figure 32: Radial mass flow rate for NGC 1530 first analyzed in Zhang & Buta (2007). The solid line is calculated using the full Fourier spectra of density and potential, and the dashed line using only the  $m=2$  components.

angular momentum density of the wave, this contributes to the damping of the wave and the secular decay of the mean stellar orbit; the second aspect is the randomization of the residual orbital energy corresponding to  $(\Omega - \Omega_p) \times L_{wave}$  (for matter inside corotation). There is a corresponding sign change for matter outside corotation). This second aspect results in the secular heating of the disk stars (which produces the age-velocity dispersion relation of the solar neighborhood stars [Z99]), as well as the energy injection into the interstellar medium to fuel a cascade process akin to the driven turbulence in fluid dynamics (which produces the Larson-Law size-line-width correlation of the interstellar clouds See Larons [1981]; Zhang et al. [2001]; Zhang [2002]; Falceta-Goncalves et al. [2015]).

Stars appear to accomplish the randomization of the orbital energy also through a kind of cascade/randomization process from the large to the progressively smaller scales. The smaller scale nonlinear exchange is nothing more than the cascaded-down version of the large-scale exchange, and does not create a new term in the energy balance equation. Another way to look at this matter is that at the QSS, the growth rate of the  $m=2$  mode is equal to the growth rate of the full nonlinear mode, since the nonlinear mode does not have an independent global amplification mechanism other than the cascading of energy from the  $m=2$  component. Therefore, at the QSS the  $m=2$  mode dissipation rate (or the  $m=2$  torque integral) is *formally* equal to the

$m=2$  growth rate<sup>12</sup>, with the  $m \neq 2$  components formally have zero growth rate as well as zero dissipation rate, even though in reality the  $m=2$  mode cannot accomplish energy dissipation without going through the cascade into nonlinear components.

This aspect of local interactions in density waves is in essence the same as what Kolmogorov had hypothesized for the energy cascade process of fully-developed fluid turbulence in the inertial range (Frisch 1995). The fact that galaxies can randomize the originally coherent orbital velocity/energy is due to the global-self-consistency constraint of the spontaneously-formed density wave mode at the quasi-steady state, which produced both the local instability/collisionless shock condition at the spiral arms, as well as the detailed correlation between kinematic and positional distributions of disk matter that enable both wave growth and damping, accompanied by dissipative basic state evolution.

In what follows we present similar  $m=2$  versus  $m=\text{full}$  mass flow rate comparison calculated using the surface density and potential obtained in our previous set of four N-body simulations. In Figures 33, 34, 35, and 36, we show the respectively calculated  $m=2$  and  $m=\text{full}$  mass flow rates for the four runs, at six different time steps, and for a duration of 3000 steps which correspond to about two and a half galactic rotation periods at radius 20, during the emergence and stabilization of the first dominant mode in each case.

From these four figures, we can tell that for every softening choice *when* the modal shape and kinematics have achieved quasi-steady state, the agreement between the  $m=2$  and  $m=\text{full}$  mass flow rates are very good, just as what we had observed for physical galaxies. Note that the QSS state can be short-lived even after its initial acquirement, because the disk surface density and modal shape continue to evolve throughout the simulation run for each case. Still, exploration into further time period of the modal evolution

---

<sup>12</sup>We say formally here because the torque integral acquires its meaning as corresponding to the dissipative angular momentum exchange between the wave and basic-state matter *only for the overall full nonlinear set of components at the QSS*. For each  $m$  component individually or for waves not at the QSS the torque integral does not uniquely predict anything, since it is a spatial average of time-dependent quantities. In other words, the torque integral, when used to predict the wave/basic-state angular momentum exchange, is a form of *closure relation* enforced through the consideration of global energy balance, at the QSS of the wave mode.

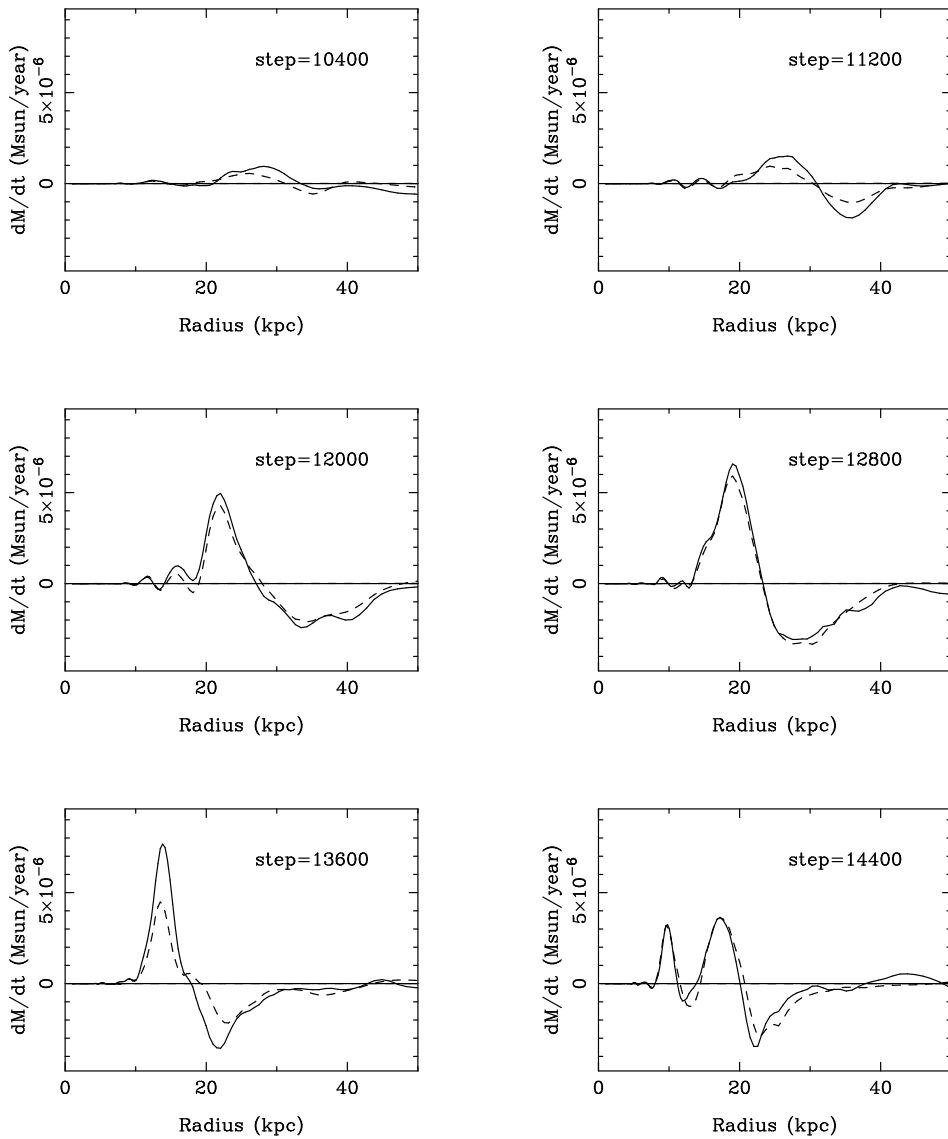


Figure 33: Radial mass flow rates for the N-body spiral mode with  $a_{soft} = 1.5$ , at six different time steps, using the full or  $m=2$  Fourier components.

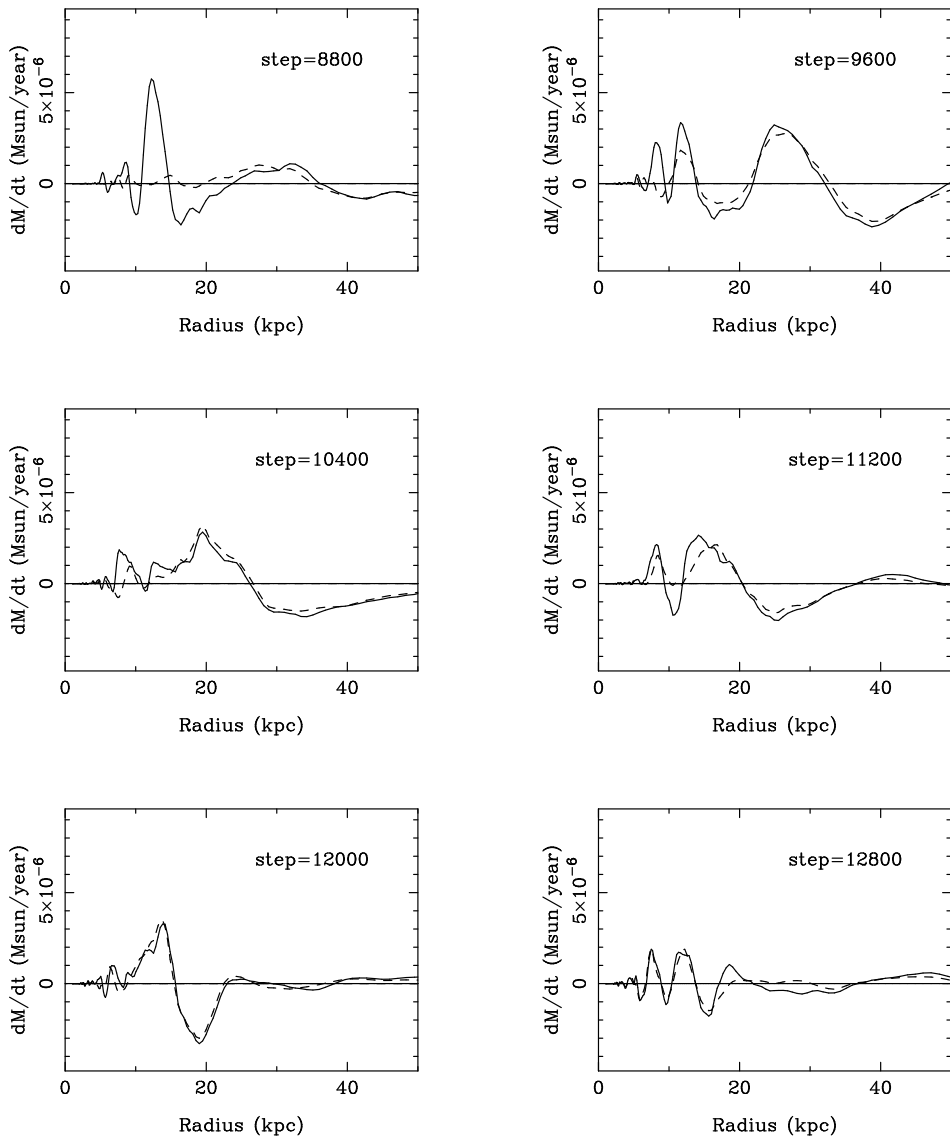


Figure 34: Radial mass flow rates for the N-body spiral mode with  $a_{\text{soft}} = 0.75$ , at six different time steps, using the full or  $m=2$  Fourier components.

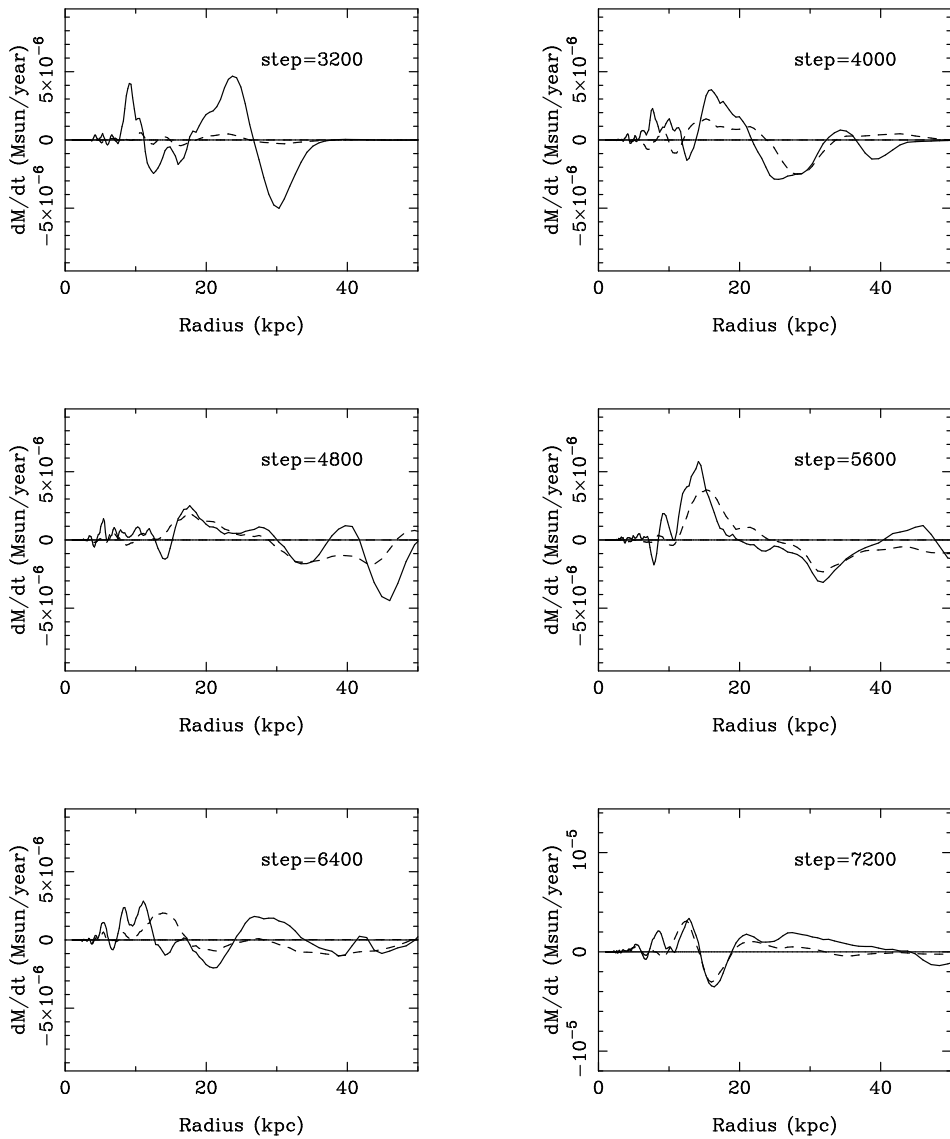


Figure 35: Radial mass flow rates for the N-body spiral mode with  $a_{\text{soft}} = 0.25$ , at six different time steps, using the full or  $m=2$  Fourier components.

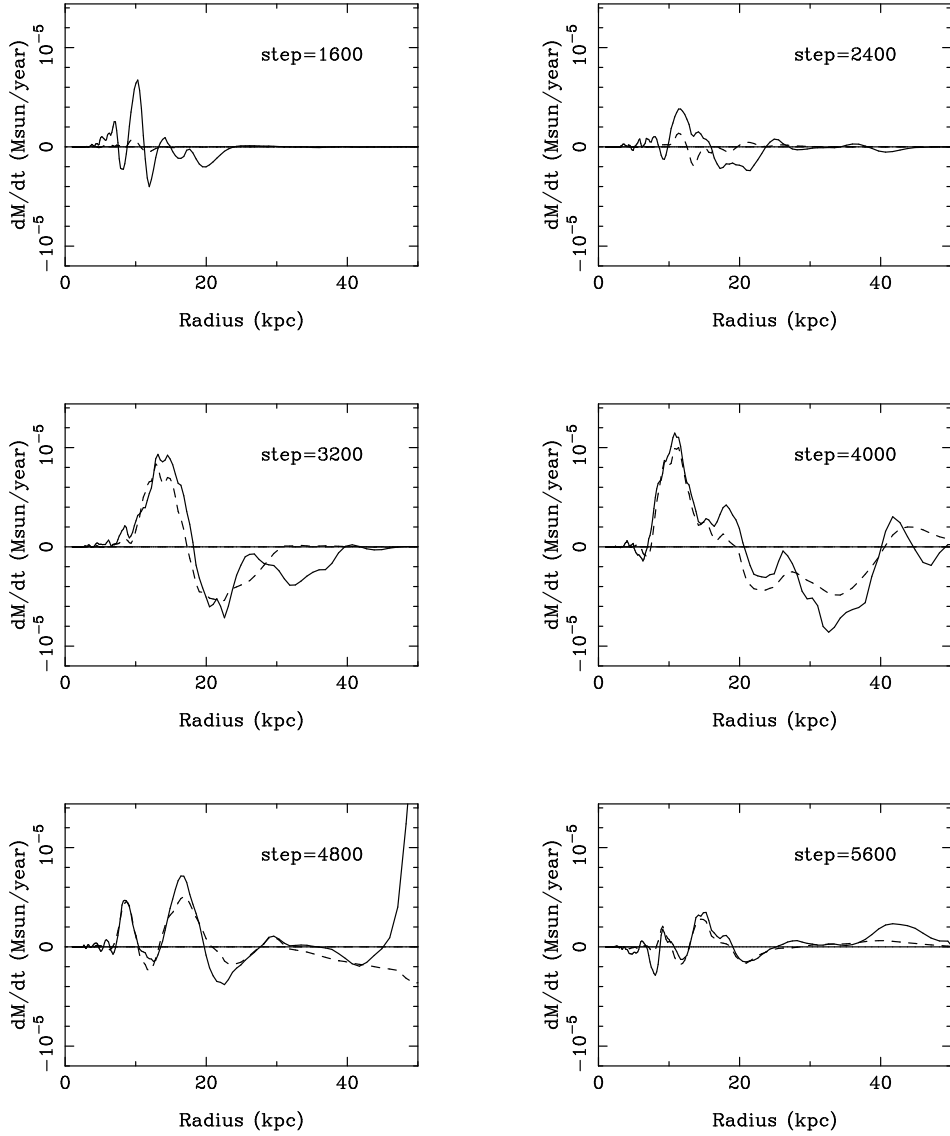


Figure 36: Radial mass flow rates for the N-body spiral mode with  $a_{soft} = 0.1$ , at six different time steps, using the full or  $m=2$  Fourier components. Note the contribution of a local instability clump in the last two frames, which have poor  $m=2$  and  $m=\text{full}$  agreement, as to be expected of this non-modal feature.

(not shown here because of the space constraint) show that a new QSS phase can once again be achieved (signified by good agreement between  $m=2$  and  $m=\text{full}$  mass flow curves) after its temporary loss as a result of the basic state evolution. In particular, the  $a_{\text{soft}} = 0.1$  run showed a most robust correlation of  $m=2$  and  $m=\text{full}$  mass flow curves throughout the simulation duration (25 galactic rotation periods at radius 20), likely a result of the fact that small softening allowed effective inter-particle correlations to quickly re-establish each new global-self-consistency state as the basic state continually to evolve.

#### *4.2. Accuracy and Implications of the Secular Radial Mass Flow Rates Obtained in N-Body Simulations*

In Appendix D, we present detailed analyses of the effect of the choice of softening parameter on the accuracy of particle-mesh N-body simulations, particularly for the polar-grid configuration. We saw there that grid noise can be of concern for small-softening, large-grid-size simulations (see also Efstathiou et al. 1985, Figure 1). For simulation parameter combinations where  $a_{\text{soft}}$  is small, the grid used is coarse, and for outer disk region where the cell size is large, grid noise has a significant impact on the accuracy of individual star's orbit – if the accuracy of individual orbit is what we are after in the simulation effort.

However, as we have shown in this paper, when simulating global density wave modes in galactic disks, grid noise does not appear to have a detrimental effect on the macroscopic properties of the modes, as well as on the *correlation* of modal parameters and their associated basic state evolution rates.

This positive outcome becomes easier to understand if we recall that in a disk system possessing collective instabilities, individual simulated orbits had long been known to diverge exponentially from true orbits in the presence of random noise, especially for simulations dealing with collective instabilities (see, e.g. Miller [1971], Pfenniger [1986], Romeo [1990], Weinberg [1993]). This exponential divergence between the simulated individual orbits and their true counterparts in globally unstable systems is present *even when large softening length is used*.

On the other hand, the collective behaviors of the modes being modelled were found not to be impacted by the microscopic inaccuracies of the simulated individual orbits – otherwise NONE of the previously published N-body simulations of galaxies containing unstable density wave patterns can be trusted! This fidelity of simulated global pattern in the face of drastic (exponential) individual orbit inaccuracy comes about because self-organized

global structures such as spiral and bar modes are “dissipative structures” in the sense of Prigogine and coworkers (Prigogine 1980), or else “strange attractors” in the sense used in nonlinear dynamical systems (Wiggins 2003 and the references therein). These systems automatically seek their attractor/modal solutions even if perturbed from corresponding nonequilibrium steady states. This property is the well-known “asymptotic stability” of the dissipative nonequilibrium quasi-steady state. In the case of galaxies possessing density wave modes, the effective collision/scattering processes at the crest of density wave patterns re-establish the correlations needed for the self-organization and collective dissipation processes, even if microscopically these orbits are not exactly what they would be for an infinite-precision calculation. From this perspective it also becomes clear why a smaller-softening choice which allows the proper establishment of correlations among particles in a simulated galaxy disk is more important than the accurate modeling of a large-softening disk which lacks the proper correlation among particles: the near-collision (or the scattering) condition allowed by small softening or efficient inter-particle interaction is what establishes the correlations among particles to allow the collective instability to successfully operate.

As we have seen, macroscopic properties of the evolution of the global density wave patterns, as well as the evolution of the basic state, are not impacted by the inaccuracies in the behavior of the individual particles’ orbits. Furthermore, if the noise in individual stellar orbits had mattered, even in physical galaxies we should not have been able to observe the beautifully organized grand-design density wave structures, since in these galaxies the stellar orbits are perturbed by chance encounters with the Giant Molecular Cloud Complexes, the tidal companion galaxies, as well as the formation of disk open- and globular star clusters. The stability of the global pattern characteristics against random fluctuation is indeed what allowed these patterns to emerge as a predominant form of organization in disk galaxies, and to have the modal characteristics correlate with that of the basic state<sup>13</sup>, rather than with the chance elements of internal and external random perturbations.

One question that may arise from examining the results of this work is that since the different softening-parameter runs gave different mass flow

---

<sup>13</sup>We recall that one of the criteria of the Hubble classification scheme is the empirically observed correlation of spiral pitch angle with the degree of prominence of the bulge. This correlation has been reproduced in the modal picture of the galactic density waves (Bertin et al. 1989a,b).

rates, what magnitude of the mass flow should we associate with the secular morphological evolution of physical galaxies?

We note that the aim of these simulations is not to derive an *absolute* mass flow rate and claim that it corresponds to that in *all* physical galaxies, but rather to demonstrate the *correlation* between the N-body simulated mass flow rate and the rate predicted by the volume-torque/mass-flow-rate equation (i.e. equation [8]). A confirmation of this correlation shows that the analytical equation predicts the correct mass flow rates for *all* ranges of the wave and basic state parameters, then the rate equation can be used in physical galaxies with the actually measured parameters for the wave and the basic state.

In the simulation results presented in this section, we had indeed shown that once the collective effects are allowed to be fully represented either by the use of sufficiently small  $a_{soft}$ , or else by the enforcement of special bi-symmetry condition, *all* of the measured mass flow rates in N-body simulations at a wide range of softening lengths have the correct correspondence with the respective analytical predictions, especially for the radial range inside corotation, which is our main interest in the secular evolution studies. Therefore, these pattern morphologies and mass flow rates can *all* find correspondence with physical galaxies of varying Hubble types. In fact, a little contemplation will show that the larger softening choices correspond to the thicker inner disk scale heights and smaller secular mass flow rates of the earlier Hubble type galaxies, whereas the smaller softening choices correspond to the thinner disk and the larger secular mass flow rates of later Hubble type galaxies (Zhang & Buta 2007, 2015).

#### *4.3. Irreversibility and Singularity-Hierarchy in Natural Systems*

Returning to some of the questions we posed in the introduction section, we note that accompanying the emergence of global patterns in an originally featureless system past its instability threshold, there is also the spontaneous emergence of new meta-laws. The torque-integral/mass-flow rate equation we have confirmed using N-body simulations in this work is an example of emergent meta-law. The original derivation of this law required the assumption of global self-consistency between the various physical processes in the galaxy (i.e. the compatibility of the energetics of the wave mode versus the energetics of the basic state, which is essentially the requirement for global energy and angular momentum conservation), as well as the assumption of

quasi-steady state of the wave mode, which is an empirically well-supported hypothesis.

Given these two very reasonable basic assumptions, the outcome of the secular evolution of the basic state of the galactic disk is inevitable, given that the pattern's matter distribution and kinematics naturally lead to the characteristic potential-density phase shift pattern which implies a secular torque action by the wave mode on the basic state, and thus secular energy and angular momentum exchange between the two components. The operation of this exchange process is necessarily dissipative (as there is the irreversible conversion of stellar orbital energy into random motion energy of stars). Furthermore, the working of the dissipation mechanism requires the presence of collisionless shock at the wave crest, or a temporary local gravitational instability at the spiral arms (Z96). This further implies that the location of the spiral arms is an effective singularity of the underlying differential (fluid) formulation (the arguments for the inevitability of the formation of this singularity or collisionless shock through the azimuthal steepening of the spiral wave solution using an Eulerian equation set was given in Z96, based on the earlier work of Lubow, Balbus, & Cowie [1986]). Z98, Z99 showed that the breakdown of the *differential* form of the Poisson equation at the density wave crest (the site of local instability and collisionless shock) is a necessary ingredient for the global self-consistency of the governing equations to be achieved. The *integral form* of the Poisson equation is what we use to obtain the global (phase shifted) perturbation potential from the perturbation density. This should come as no surprise, since we know that across any hydrodynamic shock, the differential formulation invariably breaks down (see, for example, Shu [1992]), and the properties of the shock-jumps are established by *enforcing global conservation relations*, just as what we have done in this work by enforcing global self-consistency requirement between the kinematics and mass distribution of the density wave mode, and between the energetics of the wave mode and the basic state of the disk (Z96, Z98).

Generalizing what we have learned in this work, we realize that in nature irreversibility may be the rule rather than the exception, even though the differential forms of governing equations that we commonly employ are all time-reversible. We now realize that these differential laws are likely to be idealizations, and their origins may be emergent under the general boundary conditions of the evolving universe. In this sense laws and meta-laws (or fundamental laws and emergent laws) have no clear distinction. It all depends

on the scale we conduct our observations and analyses in.

We also realize that effective singularity hierarchies (as reflected, for example, in the spontaneous emergence of density wave modes, and the attainment of new closure relations at the QSS) may be the general mechanism nature employs to separate the different domains of physical and biological sciences. Within a given hierarchy, deductive approach may be used to arrive at new inferences. However, when we are crossing the boundary of a given hierarchy (such as in the study of the emergence and maintenance of global spiral modes, as well as the secular evolution of the basic state as a result of the interaction with these modes), we need to rely on empirical evidence (such as the QSS hypothesis of the mode), meta-principles (such as the second law of thermodynamics and the theory of dissipative structures), as well as reasonable global closure relations (such as global energy and angular momentum balance considerations) in order to establish a new axiomatic structure for the subsequent analyses.

With the guidance of these general principles, we can then explore the detailed workings of the various facets of the proposed new paradigm (in the case of spiral galaxies, this involves the discoveries of the mechanisms of wave mode amplification through over-reflection and feedback; wave stabilization through damping by the basic state energy and angular momentum input; the realization of local mechanisms of dissipation or energy cascade by the action of collisionless shocks; the demonstration of the presence of potential-density phase shift in a self-sustained density wave mode by both the integral form of the Poisson equation and the equations-of-motion of disk matter).

We now also have a tentative answer to the one question that Feynman raised that we had quoted in the Introduction of this paper: Schrodinger's equation most likely does not *directly* predict the existence of frog, musical composers, and morality. Since the physical universe is organized in a hierarchical fashion with effective singularities separating the different hierarchies, and since emergent laws governing the higher level phenomena cannot be *deductively* derived from the lower level "fundamental laws", the claim that complex phenomena of the universe can be logically derived from a simple set of fundamental equations is unfounded. Instead, the differential forms of equations governing given regimes of physics are expected to be idealizations that have limited range of applicability, and will break down at instability/singularity front of the next emerging hierarchy. In such cases, guided by empirical evidence and physical intuition, new global-self-consistency or closure relations, and new meta laws (formulated perhaps as a new set of dif-

ferential equations with their new range of applicability) need to be obtained to guide the analyses.

The universe since the Big Bang is in a process of irreversible evolution. If we take into account the subtleties of quantum mechanics, no process is truly reversible (i.e. no physical system can become truly isolated). Yet we have learned in this work that some processes are more irreversible than others, i.e., those that involve self-organized structures that drastically increase the rate of entropy production generate levels of irreversibility exponentially faster than processes that are passive. Dissipation is an important element of the formation of nonequilibrium self-organized structure because it helps to stabilize the dynamical equilibrium state (as highlighted by the fluctuation-dissipation theorem) by damping out random noise fluctuations.

## 5. CONCLUSIONS

The low radial mass rates found in the past N-body simulations of disk galaxies had cast doubts on the effectiveness of secular evolution as an important dynamical process for the morphological transformation of galaxies along the Hubble sequence. In this work it is shown that such low numerical mass flow rates were chiefly the result of the artificial “softening” of gravity which is a common practice in galaxy simulations to avoid the rapid relaxations caused by the used of smaller number of particles compared to that in physical galaxies. By decreasing the amount of softening and simultaneously increasing the number of simulation particles, as well as increasing the grid and time resolution, realistic levels of mass inflow comparable to those obtained for physical galaxies are now achievable in N-body simulations, and these mass flow rates are shown to agree with theoretical predictions using the density wave parameters obtained in the same simulations. The results of this study thus support the importance of secular evolution, in particular *radial stellar mass accretion*, as an extremely relevant dynamical process in transforming the morphologies of galaxies during the past Hubble time. The exploration of the process of the emergence and maintenance of density wave modes as an example of “dissipative structures” also sheds light on more general questions regarding the emergence and the role of ordered hierarchy of structures and laws in the evolution of the universe.

## REFERENCES

- Anderson, P.W. 1972, *Science*, 177, 393
- Antonov, V.A. 1962, *Vest. Leningr. Gos. Univ.*, 7, 135
- Balogh, A., Treumann, R.A. 2013, *Physics of Collision Shocks* (New York: Springer)
- Bertin, G., Lin, C. C., Lowe, S. A., & Thurstans, R. P. 1989a, *ApJ*, 338, 78
- Bertin, G., Lin, C. C., Lowe, S. A., & Thurstans, R. P. 1989b, *ApJ*, 338, 104
- Binney, J., & Tremaine, S. *Galactic Dynamics*, (Princeton: PUP)
- Buta, R., & Zhang, X. 2009, *ApJS*, 182, 559
- Donner, K.J., & Thomasson, M. 1994, *A&A* 290, 785 (DT94)
- Efstathiou, G., David, M., Frenk, C.S., & White, S.D.M. 1985, *ApJS*, 57, 241
- Elmegreen, B.G., & Elmegreen, D.M. 1983, *ApJ*, 267, 31
- Elmegreen, B.G., & Elmegreen, D.M. 1989, in *Evolutionary Phenomena in Galaxies*, eds. J.E. Beckman & B.E.J. Pagel (Cambridge: CUP), 83
- Feynman, R.P., Leighton, R.B., & Sands, M. 1963, *The Feynman Lectures on Physics* vol. I, 7-7
- Feynman, R.P., Leighton, R.B., & Sands, M. 1964, *The Feynman Lectures on Physics* vol. II, 41-12
- Falceta-Goncalves, D., Bonnell, I., Kowal, G., Lepine, J.R.D., & Braga, C.A.S. 2015, *MNRAS*, 446, 973
- Frisch, U. 1995, *Turbulence: The Legacy of A.N. Kolmogorov* (Cambridge: CUP)
- Haan, S. et al. 2009, *ApJ*, 692, 1623
- Hockney, R.W., & Eastwood, J.W. 1988, *Computer Simulation Using Particles*
- Kalnajs, A.J. 1965, *Ph.D. thesis*, Harvard Univ.
- Kalnajs, A. J. 1972, *Astrop. Lett.*, 11, 41
- Kormendy, J. 1979, *ApJ* 227, 714
- Kormendy, J., & Kennicutt, R. 2004, *ARA&A*, 42, 603

- Kreuzer, H.J. 1981, *Nonequilibrium Thermodynamics and its Statistical Foundations*, (Oxford: OUP)
- Larson, R.B. 1981, *MNRAS*, 194, 809
- Lin, C. C., & Lau, Y. Y. 1979, *Stu. Appl. Math.*, 60, p. 97
- Lin, C. C., & Shu, F. H. 1964, *ApJ*, 140, 646
- Lindblad, B. 1963, *Stockholms Obs. Ann.*, 22, 5
- Lynden-Bell, D., & Kalnajs, A. 1972, *MNRAS*, 157, 1
- Lubow, S. H., Balbus, S. A., & Cowie L. L. 1986, *ApJ*, 309, 496
- Lynden-Bell, D., & Wood, R. 1968, *MNRAS*, 138, 495
- Mark, J.W.-K. 1976, *ApJ*, 205, 363
- Martinez-Garcia, E.E., Gonzalez-Lopezlira, R.A., & Bruzuel, A.G. 2009, *ApJ*, 694, 512
- Martinez-Garcia, E.E., Gonzalez-Lopezlira, R.A., & Bruzuel, A.G. 2011, *ApJ*, 734, 122
- Miller, R.H. 1971, *J. Comp. Phys.* 73, 90
- Miller, R.H. 1976, *J. Comp. Phys.* 21, 400
- Pfenniger, D. 1986, *A&A* 165, 74
- Prigogine, I. 1980, *From Being to Becoming* (New York: Freeman)
- Romeo, A. 1990, *Ph.D. Thesis*, ISAS
- Romeo, A. 1994, *A&A* 286, 799
- Romeo, A. 1997, *A&A* 324, 523
- Romeo, A. 1998, *A&A* 335, 922
- Rybicki, G.B. 1971, *Ap&SS* 14, 15
- Sellwood, J.A. 1987, *ARA&A* 25, 151
- Shu, F.S. 1992, *The Physics of Astrophysics*, vol. 2 (Mill Valley: Univ. Sci. Books)
- Sparke, L.S., & Sellwood, J.A. 1987, *MNRAS*, 225, 653
- Thomasson, M. 1989, *Research Report*, No. 162, Dept. Radio and Space Science with Onsala Space Observatory, Chalmers Univ. of Techn., Goteborg
- Thomasson, M., Donner, K.J., & Elmegreen, B.G. 1991, *A&A*, 250, 316
- Toomre. A. 1981, in *Structure and Dynamics of Normal Galaxies*, eds. S.M. Fall & D. Lynden-Bell (Cambridge: CUP), 111

- Weinberg, M. 1993, *ApJ* 410, 543  
 White, R.L. 1988, *ApJ* 330, 26  
 Wiggins, S. 2003, *Introduction to Applied Nonlinear Dynamical Systems and Chaos*, 2nd ed. (New York: Springer)  
 Zhang, X. 1996, *ApJ* 457, 125 (Z96)  
 Zhang, X. 1998, *ApJ* 499, 93 (Z98)  
 Zhang, X. 1999, *ApJ* 518, 613 (Z99)  
 Zhang, X. 2002, *Ap&SS* 281, 281  
 Zhang, X. 2003, *Journal of the Korean Astronomical Society*, 36, 223  
 Zhang, X. 2008, *PASP*, 120, 121  
 Zhang, X. & Buta, R. 2007, *AJ* 133, 2584  
 Zhang, X. & Buta, R. 2015, *NewA*, 34, 65  
 Zhang, X., Lee, Y., Bolatto, A., & Stark, A. A. 2001, *ApJ*, 553, 274

## APPENDIX A: POTENTIAL-DENSITY PHASE SHIFTS AND RADIAL MASS FLOW RATES

The original derivation of the collective dissipation mechanism responsible for the secular redistribution of galaxy disk mass can be found in Z96, Z98, Z99. Here we give a brief summary of the analytical results used in the main text of the current paper.

For a disk galaxy with non-axisymmetric density and potential perturbations of  $\Sigma_1$  and  $\mathcal{V}_1$ , respectively, the (z-component) torque applied by the total potential on the material at a unit-width annular ring at a galactic distance  $R$  (which, at the quasi-steady state of the density wave mode, is equal to the averaged rate of angular momentum flow from the wave to the disk material) is

$$T(R) = -R \int_0^{2\pi} \Sigma_1(R, \phi) \frac{\partial \mathcal{V}_1(R, \phi)}{\partial \phi} d\phi = 2\pi R \overline{\frac{dL}{dt}}(R), \quad (2)$$

where  $L$  is the angular momentum density of the disk material. It can be shown that the only way for this torque and angular momentum exchange expression to be non-zero is to have the potential perturbation phase-shifted in azimuth from the density perturbation, which is naturally satisfied by a spontaneously formed, skewed density wave mode (Z96). For such a mode

the phase shift distribution versus galactic radius is of a characteristic two-humped shape, positive inside corotation and negative outside, with the zero-crossing of phase shift versus galactic radius curve happen at corotation radius.

Based on the above torque expression, the equivalent phase shift  $\phi_0$  between two nonlinear wave forms is defined as (1998),

$$\phi_0 = \frac{1}{m} \sin^{-1} \left( \frac{1}{m} \frac{\int_0^{2\pi} \Sigma_1 \frac{\partial \mathcal{V}_1}{\partial \phi} d\phi}{\sqrt{\int_0^{2\pi} \mathcal{V}_1^2 d\phi} \sqrt{\int_0^{2\pi} \Sigma_1^2 d\phi}} \right), \quad (3)$$

where  $m$  is the number of spiral arms, and the sign of the phase shift is defined such that the phase shift is positive when the potential lags the density in the direction of galactic rotation. The equivalent phase shift is the amount of phase shift which would be present between two sinusoidal wave forms if each is endowed with the same energy as the corresponding nonlinear wave form, and which would lead to the same value for the torque integral as would the nonlinear waveforms. Note that in the above expression the perturbation waveforms must have their azimuthal mean values subtracted.

The (inward) radial mass accretion rate at a galactic radius  $R$  is related to the mean orbital decay rate  $-dR/dt$  of an average star through

$$\frac{dM(R)}{dt} = -\frac{dR}{dt} 2\pi R \Sigma_0(R) \quad (4)$$

where  $\Sigma_0(R)$  is the mean surface density of the basic state of the disk at radius  $R$ .

We also know that the mean orbital increase rate of a single star  $dR/dt$  is related to its angular momentum gain rate  $dL^*/dt$  through

$$\frac{dL^*}{dt} = V_c M_* \frac{dR}{dt} \quad (5)$$

where  $V_c$  is the mean circular velocity at radius  $R$ , and  $M_*$  the mass of the relevant star.

Now we have also

$$\frac{dL^*}{dt} = \overline{\frac{dL}{dt}}(R) \frac{M_*}{\Sigma_0} \quad (6)$$

where  $\overline{\frac{dL}{dt}}(R)$  is the angular momentum gain rate of the basic state disk matter per unit area at radius  $R$ .

Since

$$\overline{\frac{dL}{dt}}(R) = -\frac{1}{2\pi} \int_0^{2\pi} \Sigma_1 \frac{\partial \mathcal{V}_1}{\partial \phi} d\phi \quad (7)$$

(Z96), we have finally

$$\frac{dM(R)}{dt} = \frac{R}{V_c} \int_0^{2\pi} \Sigma_1 \frac{\partial \mathcal{V}_1}{\partial \phi} d\phi \quad (8)$$

where the subscript 1 denotes the perturbation quantities. This result, even though derived through the stellar orbital decay rate, is in fact general, and can be applied to the mass accretion rate of both stars and gas, as long as the relevant perturbation surface density is used. The perturbation potential field used in the calculations needs to be the total potential (i.e. stars plus gas), however. We see also from the expressions of mass flow (equation 8) and phase shift (equation 3) that they share *the same zero crossings* (that of the zero crossings in the torque integral expression), but have different radial amplitude modulations.

From the above equation, it can be also shown that for waves with moderate pitch angles, the mass flow rate can be further written in terms of the parameters of the wave and basic state (Z98 §5.1):

$$\frac{dM(R)}{dt} = \pi F^2 R V_c \tan(i) \sin(m\phi_0) \Sigma_0, \quad (9)$$

where  $F$  is the fractional amplitude of the wave (defined as the *geometric mean* of the fractional potential wave amplitude and fractional density wave amplitude),  $i$  is the pitch angle of the wave,  $m$  is the number of arms (usually taken to be 2),  $\phi_0$  is the azimuthal potential-density phase shift, and  $\Sigma_0$  is the local surface density of the basic state mass distribution.

For the phase shift distribution of a spontaneously formed spiral or bar mode, the direction of torque (or the sign of phase shift) leads to mass inflow inside corotation and outflow outside corotation (Z96, Z98). The existence of the phase shift distribution across the galactic radius for a spontaneously formed density wave mode thus serves as the natural engine for the secular evolution of galaxies. The role of the density wave pattern is functional as well as structural, and the most important function of it is to accelerate the entropy evolution of the parent system, as is the case for all dissipative structures (Prigogine 1980).

## APPENDIX B CHOICE OF BASIC STATE PARAMETERS

We have chosen to use normalized units in the N-body calculations for this work, similar to that used in Donner & Thomasson (1994). In these units, the total mass of the disk, including the active disk mass  $m_d$ , the inert halo mass  $m_h$ , and the inert bulge mass  $m_b$ , sums to 1, i.e.

$$m_{total} = m_d + m_h + m_b = 1. \quad (10)$$

Z96 used the set of mass ratios  $m_d : m_h : m_b = 0.5 : 0.4 : 0.1$ , the same as used in Donner & Thomasson (1994), whereas Z98, Z99 used an alternative set of  $m_d : m_h : m_b = 0.4 : 0.5 : 0.1$ , which is what is used for the basic state in the current paper. This slightly differing choice in the second set allows a more long lasting dominant mode to be present during the simulation run.

The disk surface density used in the simulations is in the form of a modified exponential (which is an exponential with a central hole, accounting for the fact that the active disk mass decreases in the center, and the mass in the central region is dominated by the bulge mass)

$$\Sigma_d(r) = \Sigma_{d0}(e^{-r/R_d} - e^{-2r/R_d}), \quad (11)$$

where we have chosen  $R_d = 10$  for the disk scale length in the normalized unit, and  $\Sigma_{d0}$  is a constant chosen to make the total disk mass of the correct amount  $m_d$  in the normalized unit. The curve for this basic state mass distribution can be found in Figure 5 and Figure 30 as the “initial” surface density distribution (solid line).

An inactive bulge and a rigid halo (i.e., used purely for their gravitational effect on the disk particles, while their own mass distributions are not recomputed as a response to the disk evolution) are also used, which are assumed to be of the regular exponential shape:

$$\Sigma_h(r) = \Sigma_{h0}e^{-r/R_h}, \quad (12)$$

$$\Sigma_b(r) = \Sigma_{b0}e^{-r/R_b}, \quad (13)$$

The scale lengths are  $R_h = 5$  and  $R_b = 1$  for the rigid halo and bulge component, respectively. These choices of the three mass components result in a nearly constant rotation curve, with velocity  $v_c \sim 0.1$  in the normalized unit for the simulation parameter choice of the main body of the paper (and double that for the grid softening test presented in Appendix D3).

The choice for the initial radial velocity dispersion for the galaxy simulations in this work leads to an initial instability parameter  $Q$  of 1.0 throughout the disk.

This particular choice of the basic state allows a resonant cavity to be set up between the corotation region (around  $r \sim 30$  in the normalized unit for largest softening run, and  $r \sim 20$  for the smallest softening run) and the inner bulge region (which serves as a  $Q$ -barrier to reflect the inwardly-propagating wave train to complete the feedback cycle), so a normal mode of the galactic disk can spontaneously emerge.

## APPENDIX C CHOICE OF SIMULATION PARAMETERS AND DESCRIPTION OF NUMERICAL PROCEDURES

The simulation grid of this work is a polar grid similar to the original one used by Miller (1976), with radial grid rings distributed in an exponential fashion, and the azimuthal grid spokes distributed in a uniform fashion, i.e.

$$r = Le^{\alpha u}, \quad (14)$$

$$\phi = \alpha v, \quad (15)$$

where  $u$  has integer values that range from 0 to  $n_u - 1$ , and  $v$  has integer values that range from 1 to  $n_v$ .  $L$  is the constant length scale factor, usually chosen to be 1 in the normalized unit, and  $\alpha = 2\pi/n_v$ .  $n_v$  is usually selected to have a power of two so as to allow the use of the FFT algorithm for force calculation in the azimuthal direction. The exponentially spaced radial grid and uniformly spaced azimuthal grid with compatible choice of  $n_u$  and  $n_v$  ensure that the grid shape remains roughly square throughout the radial range of a galaxy disk (one of the main reasons for adopting an exponentially spaced radial grid). This choice of grid spacings also naturally matches the mass density distribution in disk galaxies, which has higher density and more finely-resolved density wave patterns in the inner disk.

Donner & Thomasson (1995) selected a grid of  $n_u = 50$  radial grid cells, and  $n_v = 64$  for the azimuthal grid cells. together with 50,000 active disk particles. These parameters have been slightly changed in the simulations of Z96 to (110, 128), and in Z96, Z98 to (55, 64). The grid used in current paper for all the simulations in the main text used a simulation grid of (220, 256), and that in Appendix D3 used a grid of size (110, 128).

The active disk particles were initially assigned on rings with constant particle number per ring ( $n_{ring} = 2 \times [n_v/2 + 1]$ ), but variable ring spacings to represent the changing disk surface density with galactic radius. The cloud-in-cell (CIC) interpolation approach (see, e.g., Hockney & Eastwood 1988, Chapter 5) is employed for grid mass assignment from the disk particle mass distribution. Fast Fourier Transform (FFT) approach was employed for grid potential calculation based on grid mass, and forces on grid points were calculated using finite difference of the grid potential. The forces on disk particles are then calculated once more through the CIC method from grid force, and these disk particles are subsequently moved around using a time-centered leap-frog scheme. Sufficient time step resolution is chosen to ensure stability and accuracy.

The length of the time step is chosen through a parameter called the number of time steps per crossing time  $S_{stpcrt}$  at a given radius (usually chosen to be  $R_d = 20$ , which is within or close to the corotation radius). This number is defined as the time steps it takes for a particle to cross the specified disk radius  $R_d$ , i.e.

$$\Delta t \cdot S_{stpcrt} = \frac{R_d}{V_c(R_d)}, \quad (16)$$

where  $\Delta t = 1$  is the normalized unit of time step, and  $V_c$  is the rotation curve value. In the original Donner & Thomasson (1994) simulation,  $S_{stpcrt}$  was chosen to be 50, which corresponds to 314 time steps per rotation period at radius 20. The same value was chosen also in Z98, Z99, though Z96 chose  $S_{stpcrt} = 100$  to correspond to the doubling of the time resolution for that particular set of simulation. We have chosen  $S_{stpcrt} = 200$  for the simulations in the main body of the text (and this corresponds to 1256 steps per rotation period), and  $S_{stpcrt} = 100$  for the simulation in Appendix D3, all at radius  $r=20$ . These  $S_{stpcrt}$  choices are made in order guarantee the numerical stability of the computation algorithm.

After  $S_{stpcrt}$  is determined, a renormalized gravitational constant  $G_{new}$  is computed and is used to replace the  $G_{old}$  in the usual Newtonian equations. The new and old gravitational constants are related through

$$G_{new} = \frac{\frac{R_d^2}{\Delta t^2 \cdot S_{stpcrt}^2}}{m_d \frac{V_d^2(R_d)}{G_{old}} + m_h \frac{V_h^2(R_d)}{G_{old}} + m_b \frac{V_b^2(R_b)}{G_{old}}}, \quad (17)$$

where  $V_d$ ,  $V_h$ ,  $V_b$  are the rotation velocity contribution of the different mass components to the total rotation curve of the galaxy, i.e.

$$m_d V_d^2 + m_h V_h^2 + m_b V_b^2 = m_{total} V_c^2 = V_c^2, \quad (18)$$

since  $m_{total} = 1$  in the normalized units. With these choices of  $\Delta t$  and  $G_{new}$  the desired  $S_{stpcrt}$  will be achieved.

Further details of the numerical procedure can be found in Miller (1976), Thomasson (1991), Donner & Thomasson (1994), as well as in Z96, Z98, Z99.

## APPENDIX D. GRID NOISE ASSOCIATED WITH THE USE OF SMALL PARTICLE SOFTENING PARAMETER

In this appendix we address the issue of whether the quality of the simulation results presented in this paper is negatively affected by the use of small particle-softening parameter  $a_{soft}$ . We will show that the *effective* disk thickness in these 2D simulations is maintained mainly by the finite size of the grid, whereas the effective inter-particle interaction which allows the operation of collective instability is enhanced by the choice of small particle softening parameter  $a_{soft}$ . The combined effects of the two, coupled with sufficient number of simulation particles and finer grid, allows the *macroscopic* features of the modes to be faithfully reproduced despite of the increased noise on individual particle's orbit.

### D1. The Differing Roles of Grid and Particle Softening

In the simulations described in the main body of this paper, while the particle softening parameter  $a_{soft}$  had been drastically reduced in some cases, the corresponding grid softening had not been reduced to a similar extent (the newer grid is only about a factor of 4 finer in linear resolution compared to that used in Z98, whereas the particle softening is reduced by a factor of 15 for the extreme choice of  $a_{soft} = 0.1$ ). It thus appears that particle softening is the main inhibitor to obtaining higher mass flow rates, the grid softening has only marginal effect: the new simulation maintaining  $a_{soft} = 1.5$  but with 4 times the linear resolution compared to Z98 did not seem to affect the mass flow rate by much, whereas decreasing  $a_{soft}$  clearly allowed the radial mass flow rate to increase (even starting with a factor of 2  $a_{soft}$  reduction, as seen in Figure 3), especially for the very central region where enough mass supply (both from the local mass surface density as well as from the mass inflow

from the outer disk) was available to support the continued mass inflow and bulge building.

Finite amount of grid softening, on the other hand, helps to maintain the desirable finite disk thickness effect in these 2D simulations. The *effective* disk thickness is the geometric mean of the particle and grid softening lengths. The finite disk thickness in our simulations manifests both in the particle-number dependence of the noise performance (Figure 5) – since relaxation in a razor-thin disk should have showed no particle-number dependence (Rybicki 1971); as well as in the longevity of the spiral-bar patterns formed – since a razor-thin disk is known to have relaxation time scale on the order of a mean orbital period (Rybicki 1971), whereas the patterns in our simulations (especially the underlying  $m=2$  component) using sufficient number of particles were shown to last more than 25 orbital periods.

In fact, Rybicki (1971) already pointed out the role of finite grid size on mimicking a finite-thickness disk. Basing his analyses on the cumulative effect of short and long-range interactions, Rybicki (1971) derived that for a numerical disk which has grid size of  $h$ , the relaxation time  $t_R$  can be expressed as

$$t_R = \frac{\lambda^3 N h t_M}{2R} \quad (19)$$

where  $\lambda$  is the ratio of random velocity  $\sigma$  to circular velocity  $V$ , i.e.  $\sigma = \lambda V$ ,  $\lambda \leq 1$ , and  $t_M$  is the orbital crossing time, i.e.  $t_M = R/V$  where  $R$  is the disk radius.

The above expression of Rybicki's is nearly equivalent to another expression derived in White (1988)

$$t_R = \frac{\sigma^3 h}{5G^2 \mu m}, \quad (20)$$

where  $\mu$  is the surface density of the disk, and  $G$  is the gravitational constant, and  $m$  is the mass of the particle. White's expression can be shown to be equivalent to Rybicki's if we replace the factor of 5 in the denominator of White's expression by a factor of  $2\pi$  in Rybicki's (or  $\pi$  if the crossing time is defined using the diameter instead of the radius of the system). Rybicki (1971) stated that the factor  $h$  is *either* the particle softening length  $a_{soft}$  *or* the grid size  $h$ , whichever is greater. Donner & Thomasson (1994), on the other hand, argued that the effective softening length is the geometric mean

of particle and grid softening, i.e.  $h = \sqrt{s^2 + a_{soft}^2}$  where  $s$  is the local grid size.

Our current work showed that finite grid size can indeed simulate a finite-thickness disk in terms of inhibiting the unwanted fast relaxation, as Rybicki had suggested, yet it does not seem to significantly diminish the desired collective dissipation effect as the choice of large particle softening length does. This is likely due to the fact that grid softening is implemented in an *anisotropic* fashion, i.e., the mass and force assignments are through the *same* Cloud-in-Cell, or CIC, interpolation scheme, which apparently helped to retain the correlated angular inhomogeneities of the particle positions and kinematics in addition to conserving momentum, in effect achieving sub-grid resolution. On the other hand, particle softening is an *isotropic* scheme that uniformly evens out the fluctuations in the force from all directions, thus has a more detrimental effect on suppressing the *correlated* collective interactions.

Figure 37 gives the relaxation time for our previous 20 million particle,  $a_{soft} = 0.1$  simulation calculated using the White (1988) expression above, with  $h$  the geometric mean of the particle and grid softening. The straight line in the figure shows the maximum time step duration (32768) used in the majority of the simulations presented in this paper. It can be seen that over most of the radial range of the simulation disk (except for the very central region) the relaxation time is much longer than the duration of the simulation, so two-body relaxation effect should be minimum, as was also borne out by the consistently vigorous spiral/bar activity shown in the main body of the paper.

## D2 Grid Noise in Particle Mesh Simulations

By choosing to use grid size larger than the particle softening parameter, we do pay a price: that of increased grid noise. This manifests as fluctuations of the interpolated forces on individual particles as we traverse grid boundaries, which can also be attributed to aliasing effect in the Fourier transform domain (Hockney & Eastwood 1988, §5-6-3 and §5-6-4). Grid noise is more pronounced for the smallest softening choices ( $a_{soft} = 0.1$ ), and it is also more pronounced in the outer disk region than in the inner disk for the polar grid used here, since the grid spacings in the outer disk are exponentially larger than in the inner disk (therefore, for all the past polar-grid simulations presented in the literature, grid noise issue was already present since

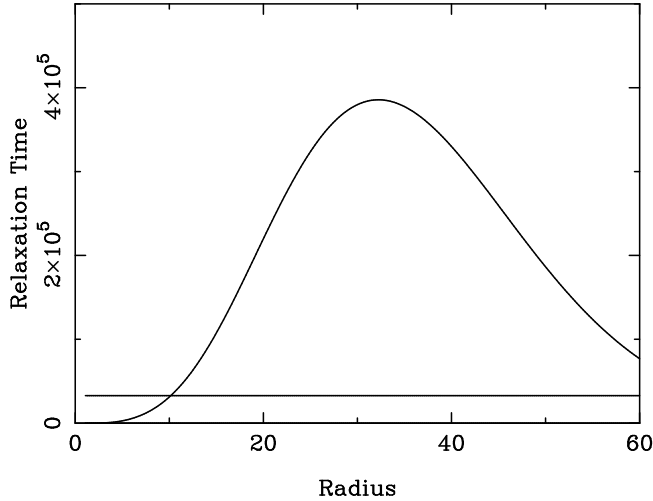


Figure 37: Relaxation time in the  $a_{soft} = 0.1$ , 20 million particle simulation. The straight line in the lower part of the figure indicates the maximum calculation duration used in the simulations here.

even when the particle softening parameter was chosen to be of the order of the grid size in the inner disk, for the outer disk region the grid size is much larger than the particle softening parameter due to the exponential growth in grid size in polar grid design).

In what follows the results of Monte Carlo calculations are presented to characterize the magnitude of the grid noise for the simulation parameters we have used in this paper. A source particle is placed at a select radial location in the disk (here we choose two radius values roughly corresponding to the inner Lindblad resonance and the corotation resonance of the mode, which give approximately the best-case and the worst-case error bounds for a modal resonant cavity between the inner disk and the corotation radius), and 100 test particles are placed at EACH of a range of distances from the source particles. Analytical results (from the Newtonian equation with softening) are compared with that obtained in the N-body (interpolated) grid force calculation scheme, averaged for the 100 test particles for each distance, at a particular choice of  $a_{soft}$ . In Figures 38, 39, and 40, we plot the noise performance of the Plummer softening scheme for the choices of softening parameters and grid sizes used in this study. Note that even though the larger softening case ( $a_{soft} = 1.5$ ) has its CR closer to 30, this large softening case has relatively small grid noise so the extent of the noise performance in that case (plotted only up to radius of 20 but can be easily extrapolated up

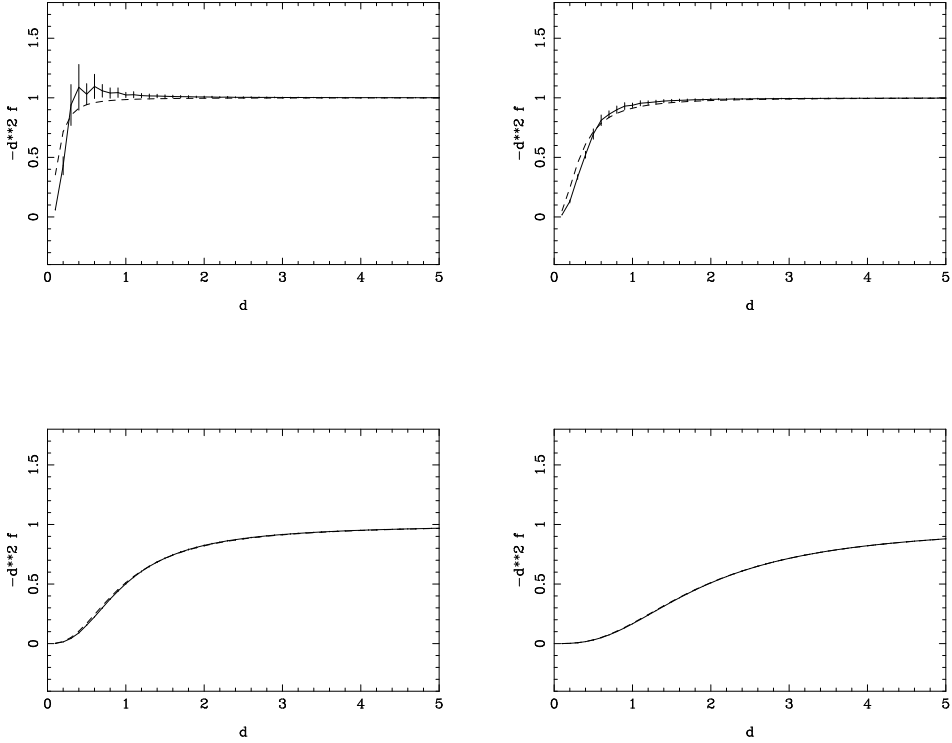


Figure 38: Grid noise estimates for N-body particle-mesh simulations using Plummer sphere softening with  $a_{soft} = 0.1$  (top left),  $a_{soft} = 0.25$  (top right),  $a_{soft} = 0.75$  (bottom left), and  $a_{soft} = 1.5$  (bottom right), respectively. All the calculations start with a point-mass source particle at  $r=10$ , and with 100 test particles at an average distance  $d$  (varying from near zero to about 5 in the normalized unit of the disk) from the source particle randomly placed within the computational grid of 220 exponentially spaced radial sections and 256 equally spaced azimuthal sections. Solid lines are expected N-body performance with  $1\sigma$  rms fluctuations, and dashed lines are the corresponding theoretical softened forces.

to 30) is no worse than the worse case scenario (for  $a_{soft} = 0.1$ ) represented in these figures. The trend of increasing grid noise with decreasing softening, with increasing galactic radius (and thus grid size), and with overall grid-coarseness, are evident in these plots.

In the main text, we have shown that despite the fluctuations of the forces caused by the increased grid noise for small softening runs, the azimuthally averaged torques and mass flow rates converge to theoretical expectations for the simulation of the self-organized density wave modes. Beside the arguments presented in the main text based on the “asymptotic stability” of the patterns amidst noise, we can also regard the mass assignment onto grid as a kind of “cluster clump” formation in real galaxies. Even though the

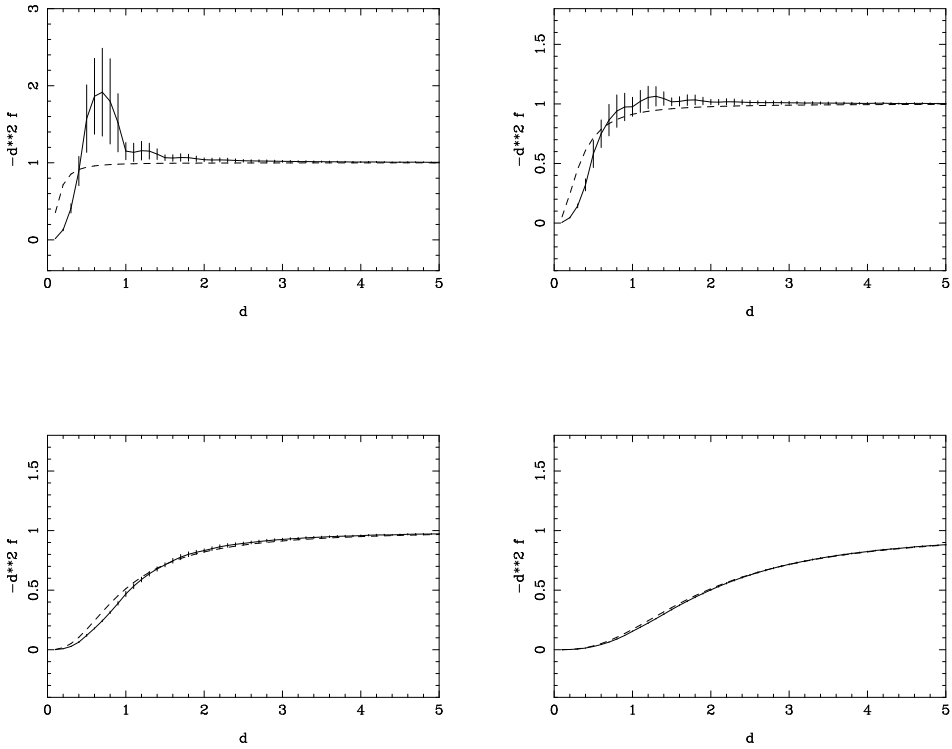


Figure 39: Grid noise estimates for N-body particle-mesh simulations using Plummer-sphere softening with  $a_{soft} = 0.1$  (top left),  $a_{soft} = 0.25$  (top right),  $a_{soft} = 0.75$  (bottom left), and  $a_{soft} = 1.5$  (bottom right), respectively. All the calculations start with a point-mass source particle at  $r=20$ , and with 100 test particles at an average distance  $d$  (varying from near zero to about 5 in the normalized unit of the disk) from the source particle randomly placed within the computational grid of 220 exponentially spaced radial sections and 256 equally spaced azimuthal sections. Solid lines are expected N-body performance with  $1\sigma$  rms fluctuations, and dashed lines are the corresponding theoretical softened forces.

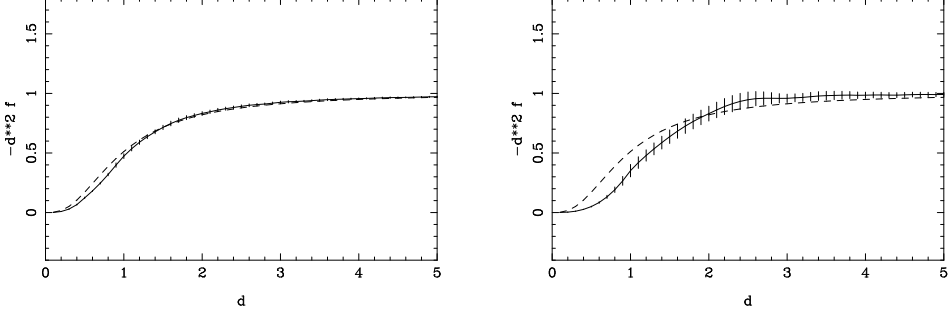


Figure 40: Grid noise estimates for N-body particle-mesh simulations using Plummer-sphere softening with  $a_{soft} = 0.75$ . All the calculations start with a point-mass source particle at  $r=10$  (left) or  $r=20$  (right), and with 100 test particles at an average distance  $d$  (varying from near zero to about 5 in the normalized unit of the disk) from the source particle, randomly placed with the computational grid of  $nr=110$  exponentially spaced radial sections and 128 equally spaced azimuthal sections. Solid lines are N-body performance with  $1 \sigma$  rms fluctuations, and dashed lines are the corresponding theoretical softened forces.

forces are of error with respect to the smooth disk model we started with, the forces are in fact *exact* with respect to the clustered mass distribution. And we know, in physical galaxies star cluster formation had no fundamental impact on a galaxy's ability to form grand design density wave patterns. Thus the errors caused by grid mass assignment should not impact modal pattern in simulated galaxies either (apart from the heating effect it caused which impacts the longevity of the mode), as we have confirmed from the simulation results in this paper.

### D3. Effects of Grid Size and Grid Noise to Mass Flow Rates In N-Body Simulations

In this section we demonstrate further that the increased mass flow rates in less-softened N-body runs are due to the collective instabilities brought about by the decreased softening, and not due to increased grid noise brought about by the same softening reduction.

The first hint for this conclusion can already be found in the previous simulation result shown in Figure 4. It was seen there that when an insufficient number of particles are used for a given  $a_{soft}$  (which generally *increases* the few-particle relaxation effect, or increases the noise), the mass inflow tapers off at an earlier time step. Whereas for very large particle numbers (which generally *decreases* the few-particle relaxation effect, or decreases the noise),

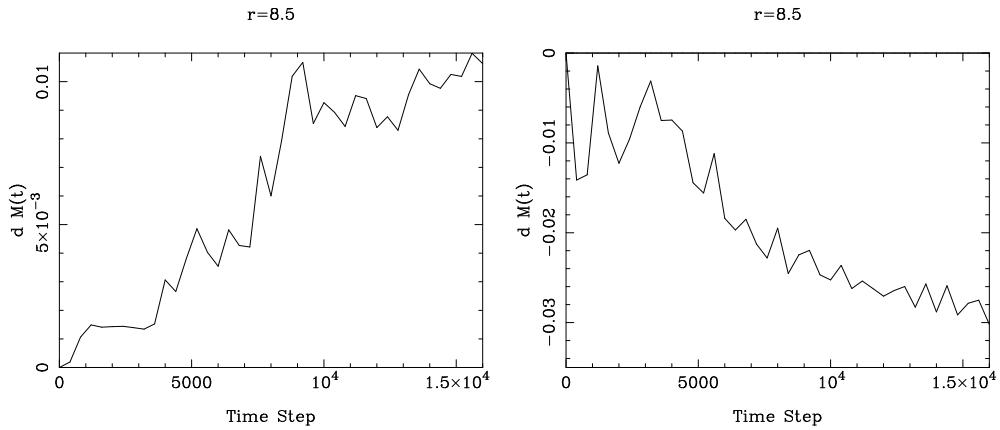


Figure 41: Time evolution of the enclosed mass for a typical location inside corotation, and a typical location outside corotation, relative to the initial  $n=0$  mass at the same respective radius, for the softening length  $a_{soft} = 0.75$  run, with a coarser mesh (110 radial sections, 128 azimuthal sections) and twice as coarse a time resolution as before.

both the spiral/bar activity and the mass inflow continues until the end of the run. This positive correlation between the number of simulation particles and the longevity of efficient mass inflow shows that noise is unlikely to be the *cause* of the increased mass flow rate. Instead, the survivability of the density wave modes appears to be the key to the continued mass inflow.

In Figures 41 and 42, we plot the same mass flow evolution as previously simulated in Figures 23 and 24 for the softening parameter choice of  $a_{soft} = 0.75$ , this time reducing the grid linear resolution by one half, and time resolution by one half correspondingly (i.e. 16384 steps here cover the same time duration in terms of pattern rotation periods as 32768 steps before). Decreasing grid resolution by one half should significantly *increase* the grid noise, from the result we presented above. Yet the results here show comparable mass flow rates compared to that obtained from the higher grid resolution ones (the slight *decrease* in mass flow rate is to the contribution of grid-softening effect to mass flow, which is apparently not as prominent as particle softening; yet even this decrease is in the opposite direction to what one would expect if grid noise is the main contributor to the *increase* in mass flow rate in simulated galaxies), especially for the first one-half of the duration of the simulation run, when the heating due to noise has not clamped the amplitude of the pattern for this coarser-grid run. This shows that we are indeed revealing the role of increased collective effects brought about by decreased particle softening, and the increased mass flow rate is

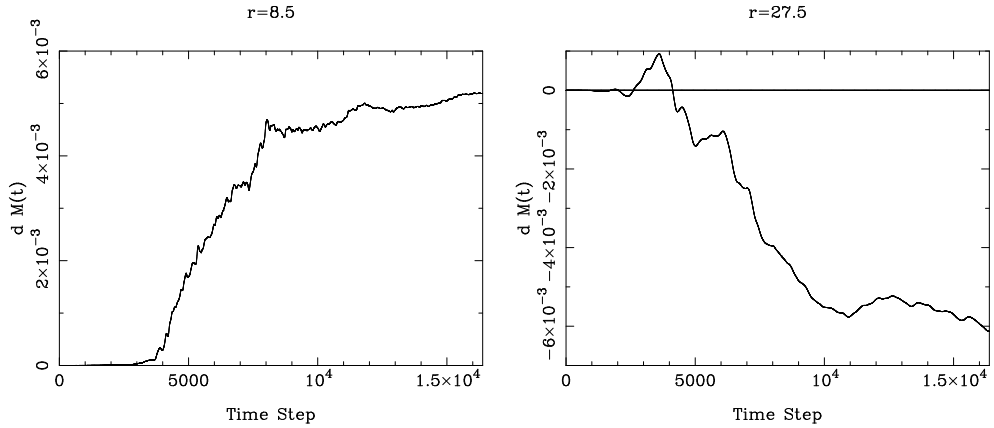


Figure 42: Predicted integrated mass evolution according to equation (8) within the two different radii, for softening length  $a_{soft} = 0.75$  run, but with a smaller grid (110 radial sections, 128 azimuthal sections) and twice as coarse a time resolution as before. The second frame (for  $r=27.5$ ) used only even harmonics in the mass flow calculation.

not due to increased grid noise (if anything, increased grid noise, and the resulting increased heating of disk particles, slightly hamper the mass flow rates in the later half of the simulation period, as evidenced by the flattening of the mass-increase curves in both Figures 41 and 42).

Therefore, we conclude that as long as our interests are in the comparison of macroscopic characteristics of the mode (equilibrium amplitude, pitch angle, potential-density phase shift and torque) in the simulations with that in theoretical predictions, as well as with that in observed galaxies, the grid noise present in simulations with smaller softening, as in the current paper, is not a debilitating inconvenience.